Eur. Phys. J. C 40, 317–332 (2005)
Digital Object Identifier (DOI) 10.1140/epjc/s2005-02122-4

THE EUROPEAN PHYSICAL JOURNAL C

Flavour–independent $\mathrm{h^0A^0}$ search and two Higgs doublet model interpretation of neutral Higgs boson searches at LEP

The OPAL Collaboration

G. Abbiendi[2], C. Ainsley[5], P.F. Åkesson[3,y], G. Alexander[22], J. Allison[16], P. Amaral[9], G. Anagnostou[1], K.J. Anderson[9], S. Asai[23], D. Axen[27], I. Bailey[26], E. Barberio[8,p], T. Barillari[32], R.J. Barlow[16], R.J. Batley[5], P. Bechtle[25], T. Behnke[25], K.W. Bell[20], P.J. Bell[1], G. Bella[22], A. Bellerive[6], G. Benelli[4], S. Bethke[32], O. Biebel[31], O. Boeriu[10], P. Bock[11], M. Boutemeur[31], S. Braibant[2], R.M. Brown[20], H.J. Burckhart[8], S. Campana[4], P. Capiluppi[2], R.K. Carnegie[6], A.A. Carter[13], J.R. Carter[5], C.Y. Chang[17], D.G. Charlton[1], C. Ciocca[2], A. Csilling[29], M. Cuffiani[2], S. Dado[21], A. De Roeck[8], E.A. De Wolf[8,s], K. Desch[25], B. Dienes[30], M. Donkers[6], J. Dubbert[31], E. Duchovni[24], G. Duckeck[31], I.P. Duerdoth[16], E. Etzion[22], F. Fabbri[2], P. Ferrari[8], F. Fiedler[31], I. Fleck[10], M. Ford[16], A. Frey[8], P. Gagnon[12], J.W. Gary[4], C. Geich-Gimbel[3], G. Giacomelli[2], P. Giacomelli[2], M. Giunta[4], J. Goldberg[21], E. Gross[24], J. Grunhaus[22], M. Gruwé[8], P.O. Günther[3], A. Gupta[9], C. Hajdu[29], M. Hamann[25], G.G. Hanson[4], A. Harel[21], M. Hauschild[8], C.M. Hawkes[1], R. Hawkings[8], R.J. Hemingway[6], G. Herten[10], R.D. Heuer[25], J.C. Hill[5], K. Hoffman[9], D. Horváth[29,c], P. Igo-Kemenes[11], K. Ishii[23], H. Jeremie[18], P. Jovanovic[1], T.R. Junk[6,i], J. Kanzaki[23,u], D. Karlen[26], K. Kawagoe[23], T. Kawamoto[23], R.K. Keeler[26], R.G. Kellogg[17], B.W. Kennedy[20], S. Kluth[32], T. Kobayashi[23], M. Kobel[3], S. Komamiya[23], T. Krämer[25], P. Krieger[6,l], J. von Krogh[11], T. Kuhl[25], M. Kupper[24], G.D. Lafferty[16], H. Landsman[21], D. Lanske[14], D. Lellouch[24], J. Letts[o], L. Levinson[24], J. Lillich[10], S.L. Lloyd[13], F.K. Loebinger[16], J. Lu[27,w], A. Ludwig[3], J. Ludwig[10], W. Mader[3,b], S. Marcellini[2], A.J. Martin[13], G. Masetti[2], T. Mashimo[23], P. Mättig[m], J. McKenna[27], R.A. McPherson[26], F. Meijers[8], W. Menges[25], F.S. Merritt[9], H. Mes[6,a], N. Meyer[25], A. Michelini[2], S. Mihara[23], G. Mikenberg[24], D.J. Miller[15], W. Mohr[10], T. Mori[23], A. Mutter[10], K. Nagai[13], I. Nakamura[23,v], H. Nanjo[23], H.A. Neal[33], R. Nisius[32], S.W. O'Neale[1,*], A. Oh[8], M.J. Oreglia[9], S. Orito[23,*], C. Pahl[32], G. Pásztor[4,g], J.R. Pater[16], J.E. Pilcher[9], J. Pinfold[28], D.E. Plane[8], O. Pooth[14], M. Przybycień[8,n], A. Quadt[3], K. Rabbertz[8,r], C. Rembser[8], P. Renkel[24], J.M. Roney[26], A.M. Rossi[2], Y. Rozen[21], K. Runge[10], K. Sachs[6], T. Saeki[23], E.K.G. Sarkisyan[8,j], A.D. Schaile[31], O. Schaile[31], P. Scharff-Hansen[8], J. Schieck[32], T. Schörner-Sadenius[8,z], M. Schröder[8], M. Schumacher[3], R. Seuster[14,f], T.G. Shears[8,h], B.C. Shen[4], P. Sherwood[15], A. Skuja[17], A.M. Smith[8], R. Sobie[26], S. Söldner-Rembold[16], F. Spano[9], A. Stahl[3,x], D. Strom[19], R. Ströhmer[31], S. Tarem[21], M. Tasevsky[8,s], R. Teuscher[9], M.A. Thomson[5], E. Torrence[19], D. Toya[23], P. Tran[4], I. Trigger[8], Z. Trócsányi[30,e], E. Tsur[22], M.F. Turner-Watson[1], I. Ueda[23], B. Ujvári[30,e], C.F. Vollmer[31], P. Vannerem[10], R. Vértesi[30,e], M. Verzocchi[17], H. Voss[8,q], J. Vossebeld[8,h], C.P. Ward[5], D.R. Ward[5], P.M. Watkins[1], A.T. Watson[1], N.K. Watson[1], P.S. Wells[8], T. Wengler[8], N. Wermes[3], G.W. Wilson[16,k], J.A. Wilson[1], G. Wolf[24], T.R. Wyatt[16], S. Yamashita[23], D. Zer-Zion[4], L. Zivkovic[24]

[1] School of Physics and Astronomy, University of Birmingham, Birmingham B15 2TT, UK
[2] Dipartimento di Fisica dell' Università di Bologna and INFN, 40126 Bologna, Italy
[3] Physikalisches Institut, Universität Bonn, 53115 Bonn, Germany
[4] Department of Physics, University of California, Riverside CA 92521, USA
[5] Cavendish Laboratory, Cambridge CB3 0HE, UK
[6] Ottawa-Carleton Institute for Physics, Department of Physics, Carleton University, Ottawa, Ontario K1S 5B6, Canada
[8] CERN, European Organisation for Nuclear Research, 1211 Geneva 23, Switzerland
[9] Enrico Fermi Institute and Department of Physics, University of Chicago, Chicago IL 60637, USA
[10] Fakultät für Physik, Albert-Ludwigs-Universität Freiburg, 79104 Freiburg, Germany
[11] Physikalisches Institut, Universität Heidelberg, 69120 Heidelberg, Germany
[12] Indiana University, Department of Physics, Bloomington IN 47405, USA
[13] Queen Mary and Westfield College, University of London, London E1 4NS, UK
[14] Technische Hochschule Aachen, III Physikalisches Institut, Sommerfeldstrasse 26–28, 52056 Aachen, Germany
[15] University College London, London WC1E 6BT, UK
[16] Department of Physics, Schuster Laboratory, The University, Manchester M13 9PL, UK
[17] Department of Physics, University of Maryland, College Park, MD 20742, USA
[18] Laboratoire de Physique Nucléaire, Université de Montréal, Montréal, Québec H3C 3J7, Canada
[19] University of Oregon, Department of Physics, Eugene OR 97403, USA
[20] CCLRC Rutherford Appleton Laboratory, Chilton, Didcot, Oxfordshire OX11 0QX, UK
[21] Department of Physics, Technion-Israel Institute of Technology, Haifa 32000, Israel

[22] Department of Physics and Astronomy, Tel Aviv University, Tel Aviv 69978, Israel
[23] International Centre for Elementary Particle Physics and Department of Physics, University of Tokyo, Tokyo 113-0033, and Kobe University, Kobe 657-8501, Japan
[24] Particle Physics Department, Weizmann Institute of Science, Rehovot 76100, Israel
[25] Universität Hamburg/DESY, Institut für Experimentalphysik, Notkestrasse 85, 22607 Hamburg, Germany
[26] University of Victoria, Department of Physics, P O Box 3055, Victoria BC V8W 3P6, Canada
[27] University of British Columbia, Department of Physics, Vancouver BC V6T 1Z1, Canada
[28] University of Alberta, Department of Physics, Edmonton AB T6G 2J1, Canada
[29] Research Institute for Particle and Nuclear Physics, 1525 Budapest, P O Box 49, Hungary
[30] Institute of Nuclear Research, 4001 Debrecen, P O Box 51, Hungary
[31] Ludwig-Maximilians-Universität München, Sektion Physik, Am Coulombwall 1, 85748 Garching, Germany
[32] Max-Planck-Institute für Physik, Föhringer Ring 6, 80805 München, Germany
[33] Yale University, Department of Physics, New Haven, CT 06520, USA

Received: 28 July 2004 / Revised version: 4 January 2005 /
Published online: 3 March 2005 –

Abstract. Upper limits on the cross-section of the pair-production process $e^+e^-\to h^0A^0$, assuming 100 % branching fraction to hadrons, are derived from a new search for the $h^0A^0\to$ hadrons final state, independently of the hadronic flavour of the decay products. This study, combined with previously published searches for the neutral Higgs bosons h^0 and A^0, is used to constrain the Type II Two Higgs Doublet Model (2HDM(II)) with no CP violation in the Higgs sector and no additional non–Standard Model particles besides the five Higgs bosons. The analysis combines LEP1 and LEP2 data collected with the OPAL detector up to the highest available centre-of-mass energies. The searches are sensitive to the h^0, $A^0\to q\bar{q}$, gg, $\tau^+\tau^-$ and $h^0\to A^0A^0$ decay modes of the Higgs bosons. A benchmark scan of the 2HDM(II) parameter space is performed. Large regions of the 2HDM(II) parameter space explored are excluded at the 95% CL in the (m_h, m_A), (m_h, tanβ) and (m_A, tanβ) planes, using both direct neutral Higgs boson searches and indirect limits derived from Standard Model high precision measurements. The region $1 \lesssim m_h \lesssim 55\,\text{GeV}$ and $3 \lesssim m_A \lesssim 63\,\text{GeV}$ is excluded at 95 % CL, independently of m_h, m_A, tanβ and for selected values of α which are representative of a complete α–scan.

1 Introduction

The data collected by the OPAL detector at LEP during the years 1999 and 2000 at centre-of-mass energies $\sqrt{s} \approx 192,\ 196,\ 200 - -209\,\text{GeV}$ are combined with the data at the Z^0 pole, $\sqrt{s} \approx 183\,\text{GeV}$ and 189 GeV, to search for neutral Higgs bosons in the framework of the Type II Two Higgs Doublet Model (2HDM(II)) with no CP violation in the Higgs sector and no additional particles besides those arising from the Higgs mechanism. This study updates the results of a previous OPAL publication [1], which included data at the Z^0 pole, $\sqrt{s} \approx 183\,\text{GeV}$ and 189 GeV.

In the minimal Standard Model (SM) the Higgs sector comprises only one complex Higgs doublet [2–4] resulting in one physical neutral Higgs scalar whose mass is a free parameter of the theory. However, it is important to study extended models containing more than one physical Higgs boson in the spectrum. In particular, Two Higgs Doublet Models (2HDMs) [5–7] are attractive extensions of the SM since they predict new phenomena with the fewest

[a] and at TRIUMF, Vancouver, Canada V6T 2A3
[b] now at University of Iowa, Dept of Physics and Astronomy, Iowa, U.S.A.
[c] and Institute of Nuclear Research, Debrecen, Hungary
[e] and Department of Experimental Physics, University of Debrecen, Hungary
[f] and MPI München
[g] and Research Institute for Particle and Nuclear Physics, Budapest, Hungary
[h] now at University of Liverpool, Dept of Physics, Liverpool L69 3BX, U.K.
[i] now at Dept. Physics, University of Illinois at Urbana-Champaign, U.S.A.
[j] and Manchester University
[k] now at University of Kansas, Dept of Physics and Astronomy, Lawrence, KS 66045, U.S.A.
[l] now at University of Toronto, Dept of Physics, Toronto, Canada
[m] current address Bergische Universität, Wuppertal, Germany
[n] now at University of Mining and Metallurgy, Cracow, Poland
[o] now at University of California, San Diego, U.S.A.
[p] now at The University of Melbourne, Victoria, Australia
[q] now at IPHE Université de Lausanne, 1015 Lausanne, Switzerland
[r] now at IEKP Universität Karlsruhe, Germany
[s] now at University of Antwerpen, Physics Department,2610 Antwerpen, Belgium; supported by Interuniversity Attraction Poles Programme – Belgian Science Policy
[u] and High Energy Accelerator Research Organisation (KEK), Tsukuba, Ibaraki, Japan
[v] now at University of Pennsylvania, Philadelphia, Pennsylvania, USA
[w] now at TRIUMF, Vancouver, Canada
[x] now at DESY Zeuthen
[y] now at CERN
[z] now at DESY
[*] Deceased

new parameters; they satisfy the constraints of $\rho \approx 1$ and the absence of tree–level flavour changing neutral currents, provided the Higgs boson fermion couplings are appropriately chosen.

In the context of 2HDMs the Higgs sector comprises five physical Higgs bosons: two neutral CP-even scalars, h^0 and H^0 (with $m_h < m_H$), one CP-odd scalar, A^0, and two charged scalars, $H^\pm$. The four Higgs boson masses are free parameters of the model.

Two Higgs Doublet Models are classified according to the Higgs boson couplings to fermions. In the Type II model the first Higgs doublet couples only to down–type fermions and the second Higgs doublet couples only to up–type fermions. In the Type I model the quarks and leptons only couple to the second Higgs doublet. The Higgs sector in the minimal supersymmetric extension of the SM [5,8] is a Type II 2HDM, in which the introduction of supersymmetry adds new particles and constrains the parameter space of the Higgs sector of the model. The 2HDM(II) Higgs potential and detailed description of the physical parameters of the model are given in [5–7].

At the centre-of-mass energies accessed by LEP, the h^0 and A^0 bosons are expected to be produced predominantly via two processes: the Higgsstrahlung process $e^+e^-\to h^0Z^0$ and the pair–production process $e^+e^-\to h^0A^0$. The cross-sections for these two processes, σ_{hZ} and σ_{hA}, are related, at tree level in the absence of initial state radiation, to the SM Higgsstrahlung production cross-section by the following relations [5]:

$$e^+e^- \to h^0Z^0 \;:\; \sigma_{hZ} = \sin^2(\beta-\alpha)\;\sigma_{HZ}^{SM}, \qquad (1)$$

$$e^+e^- \to h^0A^0 \;:\; \sigma_{hA} = \cos^2(\beta-\alpha)\;\bar{\lambda}\;\sigma_{HZ}^{SM}\,, \qquad (2)$$

where σ_{HZ}^{SM} is the Higgsstrahlung cross-section for the SM process $e^+e^-\to H^0_{SM}Z^0$, α and β are both Higgs mixing angles where $\tan\beta$ is defined in terms of the ratio of the vacuum expectation values, v_1 and v_2, of the two scalar fields, $\tan\beta = v_2/v_1$ and $\bar{\lambda} = \lambda_{Ah}^{3/2}/\{\lambda_{Zh}^{1/2}[12m_Z^2/s+\lambda_{Zh}]\}$ accounts for the suppression of the P-wave cross-section near the threshold, with $\lambda_{ij} = (1-m_i^2/s+m_j^2/s)^2 - 4m_i^2m_j^2/s^2$ being the two–particle phase–space factor. Equations (1) and (2) only serve to introduce $\sin^2(\beta-\alpha)$ and $\cos^2(\beta-\alpha)$, the initial–state radiation process $e^+e^-\to h^0A^0\gamma$ exists at tree–level and contributes to the inclusive h^0A^0 cross–section. In doing the scan of the parameter space of the model the production cross–sections are calculated taking into account initial state radiation and radiative corrections as explained in Sect. 7.

In a 2HDM the production cross-sections and Higgs boson decay branching ratios are predicted for a given set of model parameters. The coefficients $\sin^2(\beta-\alpha)$ and $\cos^2(\beta-\alpha)$ which appear in (1) and (2) determine the production cross-sections. The decay branching ratios to the various final states are also determined by α and β. In the 2HDM(II) the tree–level couplings of the h^0 and A^0 bosons to the up– and down–type quarks relative to the couplings of the SM Higgs boson to the corresponding fermions are [5]

$$h^0c\bar{c} : \frac{\cos\alpha}{\sin\beta}, \qquad h^0b\bar{b} : -\frac{\sin\alpha}{\cos\beta},$$
$$A^0c\bar{c} : \cot\beta, \qquad A^0b\bar{b} : \tan\beta\,, \qquad (3)$$

justifying a scan over both angles when combining the different production cross-section mechanisms and final states.

This paper presents a scan over the 2HDM(II) parameter space. Each of the scanned points is considered as an independent scenario within the 2HDM(II), and results are provided for each point in the (m_h, m_A, $\tan\beta$, α) space. The masses m_h and m_A are varied such that the kinematically accessible range at LEP is fully covered. The choice $0 < \beta < \pi/2$ is derived from $v_1, v_2 > 0$ which in the MSSM implies that $-\pi/2 \le \alpha \le 0$ [9]. This range was studied in [1] to cover an MSSM oriented 2HDM(II). However, to completely cover any 2HDM(II), α has to be varied over an arbitrarily chosen angular range of π. In order to extend the analysis done in [1] beyond the MSSM–like 2HDM(II), the domain $-\pi/2 \le \alpha \le \pi/2$ is explored in the present study.

The final states of the processes (1) and (2) are determined by the decays of the Z^0, h^0 and A^0 bosons. Higgs bosons couple to fermions with a strength proportional to the fermion mass, favouring the decays into pairs of b–quarks and tau leptons at LEP energies. However, with values of α and $\tan\beta$ close to zero the decays into up–type quarks and gluons through quark loops become dominant, motivating the inclusion of flavour–independent analyses.

Section 2 contains a short description of the OPAL detector and the Monte Carlo simulations used. A new analysis at the highest LEP energies with improved sensitivity for the process $e^+e^-\to h^0A^0\to$ hadrons, independently of the hadronic flavour of the decay products, is presented in Sect. 3. In Sect. 4 the confidence level calculation method is described. A limit on the cross-section of the pair-production process $e^+e^-\to h^0A^0$, assuming 100 % branching fraction to hadrons, is given in Sect. 5. The data samples, the final states studied and the external constraints used for the 2HDM(II) interpretation are described in Sect. 6. The 2HDM(II) interpretation of the searches is presented in Sect. 7, and in Sect. 8 the results are summarised and conclusions are drawn.

2 OPAL detector and Monte Carlo samples

The OPAL detector [10] has nearly complete solid angle coverage and excellent hermeticity. The innermost detector of the central tracking is a high-resolution silicon microstrip vertex detector [11] which lies immediately outside of the beam pipe. The silicon microvertex detector is surrounded by a high precision vertex drift chamber, a large volume jet chamber, and z–chambers to measure the z coordinates[1] of tracks, all in a uniform 0.435 T axial magnetic field.

[1] OPAL uses a right-handed coordinate system where the $+z$ direction is along the electron beam and where $+x$ points to the centre of the LEP ring. The polar angle, θ, is defined with respect to the $+z$ direction and the azimuthal angle, ϕ, with respect to the horizontal, $+x$ direction.

Table 1. The integrated luminosities, $\mathcal{L}$, at each centre-of-mass energy, $\sqrt{s}$, used for the flavour–independent $h^0A^0\rightarrow$ hadrons search

Year	$\sqrt{s}$ [GeV]	$\mathcal{L}$ [pb^{-1}]
1999	191.6	28.9
1999	195.5	74.8
1999	199.5	77.2
1999	201.6	36.1
2000	206.0	208

The lead-glass electromagnetic calorimeter and the presampler are located outside the magnet coil. It provides, in combination with a number of forward detectors and the silicon-tungsten luminometer [12], geometrical acceptance down to 25 mrad from the beam direction. The silicon-tungsten luminometer serves to measure the integrated luminosity using small angle Bhabha scattering events [13]. The magnet return yoke is instrumented with streamer tubes and thin gap chambers for hadron calorimetry and is surrounded by several layers of muon chambers.

Events are reconstructed from charged particle tracks and energy deposits ("clusters") in the electromagnetic and hadron calorimeters. The tracks and clusters must pass a set of quality requirements similar to those used in previous OPAL Higgs boson searches [14]. Charged particle tracks and energy clusters, satisfying these requirements, are associated to form "energy flow objects". A matching algorithm is employed to reduce double counting of energy in cases where charged tracks point toward electromagnetic clusters [14]. The energy flow objects are then grouped into jets and contribute to the total energy and momentum of the event. The association into jets is performed by the Durham jet finder algorithm [15].

For the $h^0A^0\rightarrow$hadrons analysis, the data are separated into four $\sqrt{s}$ bins for the 1999 data, with average $\sqrt{s}$ values of approximately 192 GeV, 196 GeV, 200 GeV, and 202 GeV. All of the data taken in the year 2000 are treated together, with an average $\sqrt{s}$ of 206 GeV. The luminosities of each of the five data samples are given in Table 1.

A variety of Monte Carlo samples has been generated in order to estimate the detection efficiencies for Higgs boson production and background from SM processes. The `HZHA` [16] Monte Carlo has been used to generate the signal for all the processes studied in this paper. In particular, Monte Carlo signal samples for the h^0A^0 channel have been generated using `HZHA` on a grid in the (m_h, m_A) plane, as shown in Fig. 1. One thousand signal Monte Carlo events are generated and simulated for each point on the grid for each of the five centre-of-mass energies given in Table 1. Samples are generated for four flavour combinations of the decays, namely $h^0A^0\rightarrow b\bar{b}b\bar{b}$, $h^0A^0\rightarrow b\bar{b}c\bar{c}$, $h^0A^0\rightarrow c\bar{c}c\bar{c}$, and $h^0A^0\rightarrow gggg$.

For the background processes the following event generators are used: `KK2f` [17] for $(Z/\gamma)^*\rightarrow q\bar{q}(\gamma)$, $\mu^+\mu^-(\gamma)$ and $\tau^+\tau^-(\gamma)$, `BHWIDE` [18] for $e^+e^-(\gamma)$ and `KORALW` [19] and `grc4f` [20] for four-fermion processes. The `KK2f` prediction for $q\bar{q}(\gamma)$ were compared to `PYTHIA` [21] and `HERWIG` [22] samples. The `KORALW` prediction for hadronic and semi-leptonic four-fermion processes (with no electron in the final state) were compared to `grc4f` samples. `JETSET` [21] is used as the principal model for fragmentation.

The detector response to the generated particles is simulated in full detail [23].

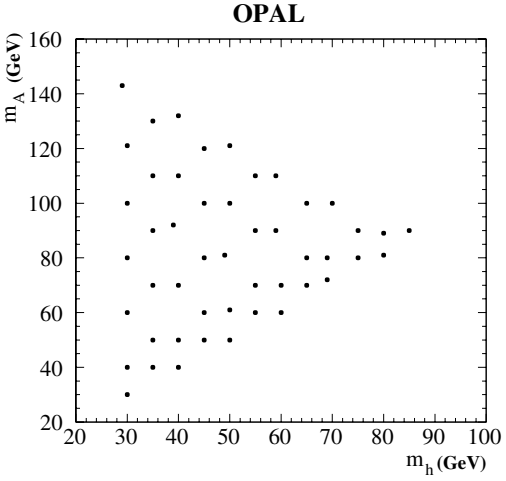

Fig. 1. The mass grid on which the signal was generated for the analysis of the data taken in 2000. A similar grid is used for the data taken in 1999

3 Flavour–independent search for $e^+e^-\rightarrow h^0A^0$

For some values of the parameters specifying a 2HDM(II), $e^+e^-\rightarrow h^0Z^0$ is suppressed, either kinematically or due to small $\sin^2(\beta-\alpha)$. The decays $h^0\rightarrow b\bar{b}$ and $A^0\rightarrow b\bar{b}$ may be also suppressed in a subset of these scenarios because of reduced couplings. In such scenarios, the largest signal for Higgs boson production may be $e^+e^-\rightarrow h^0A^0$ where both the h^0 and the A^0 decay hadronically, but not necessarily to $b\bar{b}$. Decays of h^0 and A^0 to gluons are also favoured for low values of α and $\tan\beta$ respectively. The final state investigated here is four well-separated jets of hadrons of any flavour. Other LEP Collaborations have developed similar searches interpreting them in different models [24].

The search presented here is based on the search procedure applied to the 189 GeV data [1]. The search is extended by including all data collected at $\sqrt{s}$= 192 to 209 GeV, and by introducing a likelihood discriminant to combine information carried by several different kinematic variables which are measured in each event. The search for $e^+e^-\rightarrow h^0A^0\rightarrow$ hadrons in [1] is combined with the present search, but the older data are not re-analysed.

The assignment of dijets in selected candidate events to the h^0 and A^0 is ambiguous. There are six possible assignments of jets to bosons. As in [1], the pairing is chosen to minimise the χ^2 of a beam energy and momentum-constrained kinematic fit to the (m_h, m_A) hypothesis under consideration. The pairing of each event therefore depends on the test masses.

The Standard Model backgrounds for $e^+e^-\to h^0A^0\to$ hadrons are large. One of the main sources is $e^+e^-\to q\bar{q}$ (approximately 18 pb for events with less than 20 % of the centre-of-mass energy in initial state radiation at $\sqrt{s}=$ 205 GeV [25]), and includes events which may have one or more initial-state-radiation photons. Much of this background only has two jets, but hard gluon radiation produces four–jet final states in a fraction of events. In general, the radiation of a gluon produces jets close in angle to other jets, and so this background tends to mimic $e^+e^-\to h^0A^0\to$ hadrons where either h^0, A^0 or both are light.

The other main source of background is the production of pairs of vector bosons which decay hadronically. The most important process is $e^+e^-\to W^+W^-\to$ hadrons (approximately 8 pb at $\sqrt{s}=$ 205 GeV [25]); the process $e^+e^-\to Z^0Z^{0(*)}\to$ hadrons contributes at a smaller level (approximately 0.5 pb at $\sqrt{s}=$ 205 GeV [25]). These background processes produce four-jet events with large invariant masses when jets are combined together in pairs. The W^+W^- background mimics a signal with $m_h \approx m_A \approx m_W$. Furthermore, because the pairing of jets to bosons is ambiguous, the W^+W^- and $Z^0Z^{0(*)}$ backgrounds can contribute everywhere in the (m_h, m_A) plane.

The event selection starts with a cut-based preselection and proceeds with a selection based on a likelihood function.

3.1 Preselection

The preselection is inspired by the Standard Model Higgs boson search in the Higgsstrahlung process in the four-jet final state [14], without the requirement that two jets are consistent with m_Z. The cuts are:

1. Events must satisfy the hadronic final-state requirement of [26]. The effective centre-of-mass energy, $\sqrt{s'}$, obtained by kinematic fits assuming that initial state radiation photons are lost in the beampipe or seen in the detector [26] must be at least 80 % of $\sqrt{s}$. The value of the jet resolution parameter, y_{34}, at which an event is reclassified from 3– to 4–jet event by the Durham algorithm [15] must exceed 0.003.
2. The C parameter, which gives a measure of the spherical shape of the event [27], must be larger than 0.25.
3. The χ^2 probability of a 4-constraint (4C) kinematic fit requiring energy and momentum conservation must be greater than 10^{-5}.
4. The event is forced to have four jets and each of the four jets must have at least one charged particle track.
5. No jet-pairing combination may have a 6-constraint (6C) kinematic fit probability greater than 0.2, where the fit constrains the total energy, momentum, and the masses of both dijets to $m_{W^\pm}$.

Table 2 shows the numbers of events passing each of the preselection requirements in the data taken in 1999 and 2000, along with the expected backgrounds and the efficiency for a signal with $m_h = 50$ GeV and $m_A = 100$ GeV. The $\ell^+\ell^-q\bar{q}$ and $\ell\nu_\ell qq$ backgrounds are expected to be small after the preselection – their numbers are included in the 4f background numbers in Table 2. The backgrounds from two-photon processes are negligible after the preselection.

Table 2. Comparison between background simulation and the data taken in 1999 and 2000. The efficiency is luminosity-weighted average for a signal with $m_h = 50$ GeV, $m_A = 100$ GeV

Cut	2f bkg	4f bkg	tot bkg	data	eff [%]
(1)	1031.6	3206.4	4238.0	4479	76.6
(2)	976.0	3203.1	4179.1	4436	76.6
(3)	887.3	2977.2	3864.5	3807	71.0
(4)	784.7	2820.2	3605.0	3580	70.4
(5)	754.3	2035.7	2789.9	2835	68.5

3.2 Likelihood selection

The following nine kinematic variables were considered in the likelihood selection:

- $\log(\Delta\chi^2(m_h,\ m_A))$. A full description of the procedure for computing this variable is given in [1], where it was used as the only discriminant variable. For each event, a 4C kinematic fit is performed, constraining the event energy and momentum to the centre-of-mass energy and momentum. The $\Delta\chi^2(m_h,\ m_A)$ value is the increase in χ^2 when imposing the m_h and m_A mass constraints on the jet pairs. The pairing is chosen to minimise $\Delta\chi^2(m_h,\ m_A)$. This is the only variable for which the value depends on the test mass combination.
- $|\cos\theta_{\rm thrust}|$, obtained from the polar angle, $\theta_{\rm thrust}$, of the thrust axis.
- The event aplanarity A. The aplanarity is defined as $\frac{3}{2}\lambda_3$, where λ_i are the eigenvalues $[\lambda_1 \geq \lambda_2 \geq \lambda_3$ with $\lambda_1 + \lambda_2 + \lambda_3 = 1]$ of the sphericity tensor $S^{\alpha\beta} = \sum_i p_i^\alpha p_i^\beta / \sum_i |\mathbf{p}_i|^2$, and is related to the transverse momentum component out of the event plane.
- $\log(y_{34})$.
- The jet-angle sum J_s [28]. This variable is the sum of the four smallest dijet angles.
- $(E_{\rm max} - E_{\rm min})/\sqrt{s}$, the difference between the energy of the most and least energetic jets, divided by the centre-of-mass energy.
- The jet-charge-signed $\cos\theta_W$. This variable is computed using the jet pairing which maximizes the 6C fit probability to the W^+W^- mass hypothesis. The quantity

$$Q_j = \sum_{i=1}^{n_{\rm tracks}} q_i \,\mathrm{sign}(p_\parallel^i)\sqrt{|p_\parallel^i|} \qquad (4)$$

  is computed for each jet j, where $n_{\rm tracks}$ is the number of tracks in the jet, q_i is the charge of the ith track in the jet, and $p_\parallel^i = \boldsymbol{p}_i \cdot \hat{n}_j$ is the parallel component of the ith track momentum along the jet axis. If jets j and k are paired together to form a W boson candidate and jets l and m are paired to form the other W boson candidate, then

$$\cos\theta_{\rm W} = \frac{(\boldsymbol{P}_j + \boldsymbol{P}_k)\cdot\hat{z}}{|\boldsymbol{P}_j + \boldsymbol{P}_k|}\,\mathrm{sign}\,(Q_j + Q_k - Q_l - Q_m)\ , \tag{5}$$

where $\boldsymbol{P}_j$ is the three-momentum of the jet j after the 4C-fit and $\hat{z}$ is the unit vector pointing along the electron beam axis. The jet-charge-signed $\cos\theta_{\rm W}$ variable, being charge sensitive, discriminates between Higgs boson associated–production and W pair–production processes in which W's are produced with a pronounced forward-backward charge asymmetry.

– $\log(W_{\rm CC03})$, the logarithm of the WW matrix element calculated by the EXCALIBUR program [29] using the CC03 set of diagrams. The four-vectors of the jets after the 4C-fit are used as inputs to the calculation. The matrix element is computed for all possible assignments of jet pairs to W bosons and the largest value is used.
– $\log(W_{\rm QCD})$, the logarithm of the $e^+e^-\to q\bar{q}\to$ four-jet matrix element [30]. The matrix element is computed for all possible permutations of jets and the largest value is used.

Reference histograms are formed for each likelihood input variable, for each signal grid point, separately for the $e^+e^-\to q\bar{q}$ background (2f), the $e^+e^-\to$ qqqq background (4f), and the expected signal, accumulating events which pass the preselection requirements. The $\ell^+\ell^-q\bar{q}$ and $\ell\nu_\ell$qq backgrounds do not contribute to the reference histograms, but are accounted for in the final background estimates in the likelihood output histograms.

Figure 2 shows the distributions of the likelihood input variables for the data collected in 1999 and 2000, the corresponding background estimate, and the expected signal for a fully gluonic decay for the hypothesis $m_{\rm h}$= 50 GeV, $m_{\rm A}$= 60 GeV.

For any point in the ($m_{\rm h}$, $m_{\rm A}$) plane within the kinematic reach of LEP, and with $m_{\rm h} > 30$ GeV and $m_{\rm A} > 30$ GeV, a separate likelihood function may be constructed from the reference histograms of the input variables. These are formed by interpolating the signal reference histograms using nearby Monte Carlo grid points. The background reference histograms must be interpolated also for the $\log(\Delta\chi^2(m_{\rm h},\ m_{\rm A}))$ variable. These interpolations make use of the method described in [31], extended to interpolate histograms which are functions of two variables, $m_{\rm h}$ and $m_{\rm A}$. The likelihood output histograms are also interpolated, separately for the signal and each background contribution, but each bin's contents is linearly interpolated between the Monte Carlo grid points. The interpolated reference histograms allow the computation of the value of the likelihood function for each candidate for each point in the ($m_{\rm h}$, $m_{\rm A}$) plane, and the interpolated signal and background likelihood histograms allow comparison of the data likelihood distribution with the signal and background predictions.

Signal events with $h^0A^0\to b\bar{b}b\bar{b}$ are easier to separate from the background than signal events with $h^0A^0\to$ gggg since the gggg case has a poorer reconstructed mass resolution which deteriorates the $\log(\Delta\chi^2(m_{\rm h},\ m_{\rm A}))$ likelihood variable. The signal reference histograms are created using samples of $h^0A^0\to b\bar{b}b\bar{b}$ signal Monte Carlo events, and the signal likelihood histograms are filled with $h^0A^0\to$ gggg events, ensuring the statistical independence of the reference and likelihood histograms, and also ensuring the conservativeness of the performance over the possible final states of the h^0 and A^0 decays.

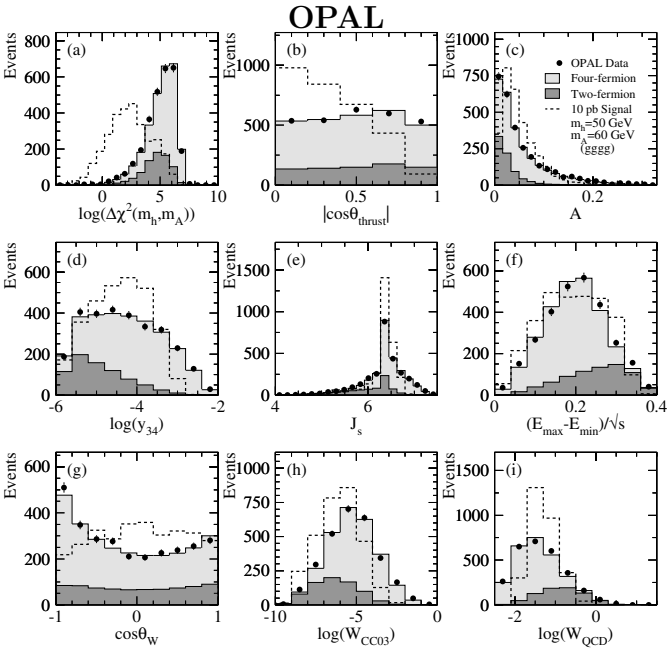

Fig. 2. Distributions of the likelihood input variables for preselected events in the flavour-independent hadronic h^0A^0 search: (a) $\log(\Delta\chi^2(m_{\rm h}, m_{\rm A}))$, (b) $|\cos\theta_{\rm thrust}|$, (c) the event aplanarity A, (d) $\log(y_{34})$, (e) J_s, (f) $(E_{\rm max} - E_{\rm min})/\sqrt{s}$, (g) the jet-charge-signed $\cos\theta_{\rm W}$, (h) $\log(\mathrm{W_{CC03}})$, and (i) $\log(\mathrm{W_{QCD}})$. The dark histograms show the two-fermion ($q\bar{q}$) background, the light histograms show the four-fermion background. The dashed histograms show a 10 pb signal of $e^+e^-\to h^0A^0\to$ gggg with $m_{\rm h}$ = 50 GeV and $m_{\rm A}$ = 60 GeV, and the points with error bars show the OPAL data collected in 1999 and 2000

Example likelihood distributions are shown in Fig. 3 for all data collected in 1999 and 2000, along with the SM background expectations and signal expectations, for three test-mass hypotheses, ($m_{\rm h}$, $m_{\rm A}$) = (50 GeV, 100 GeV), (50 GeV, 60 GeV), and (30 GeV, 60 GeV). The corresponding distributions of $\log(\Delta\chi^2(m_{\rm h},\ m_{\rm A}))$ are also shown to illustrate how the distributions of the signal, the expected backgrounds, and the candidates change with the test-mass hypothesis.

To increase the sensitivity of the search only events having a likelihood of at least 0.8 are considered in the following, independently of the test-mass hypothesis.

3.3 Systematic uncertainties

The systematic uncertainties are evaluated for the number of events passing the likelihood cut. Correlations between the uncertainties on the signal and background rates, as well as between samples taken at different centre-of-mass energies are evaluated and used in the computation of the confidence levels. The effect of simulating all year 2000

Table 3. The expected Standard Model backgrounds, observed data counts, and expected signal efficiencies for the flavour–independent h^0A^0 search as a function of the test mass hypotheses. All data collected in 1999 and 2000 are combined, and the signal efficiencies are luminosity-weighted averages. The efficiencies are listed separately for gggg, $c\bar{c}c\bar{c}$, $b\bar{b}b\bar{b}$ and $b\bar{b}c\bar{c}$ decay hypotheses. The errors given in table are statistical and systematic added in quadrature

m_h [GeV]	m_A [GeV]	2f bkg	4f bkg	total bkg	data	eff [%] gggg	eff [%] $c\bar{c}c\bar{c}$	eff [%] $b\bar{b}b\bar{b}$	eff [%] $b\bar{b}c\bar{c}$
30.0	30.0	27.0	6.1	33.1±3.1	20	1.9±0.5	2.1	1.7	1.0
40.0	30.0	42.1	11.8	53.9±5.1	42	12.1±1.4	13.7	12.2	13.9
60.0	30.0	24.1	15.2	39.2±3.7	43	26.6±2.4	27.7	30.7	29.6
80.0	30.0	16.6	22.7	39.3±3.7	46	22.0±2.1	30.1	27.4	32.4
100.0	30.0	15.3	48.2	63.5±6.0	69	16.4±1.7	22.9	24.1	22.9
120.0	30.0	12.7	34.6	47.3±4.4	59	8.8±1.1	20.1	17.9	24.3
140.0	30.0	11.3	19.3	30.6±2.9	37	3.7±0.7	8.3	8.8	7.7
40.0	40.0	29.5	15.1	44.6±4.2	32	22.1±2.1	22.7	22.3	19.1
50.0	40.0	33.0	32.1	65.1±6.1	64	36.1±3.0	36.4	33.6	36.0
70.0	40.0	19.4	34.5	53.8±5.1	46	26.7±2.4	35.8	34.6	33.7
92.0	40.0	15.7	59.1	74.8±7.0	82	17.8±1.8	28.4	24.7	26.4
110.0	40.0	14.9	58.2	73.1±6.9	74	14.7±1.6	22.9	25.7	22.6
130.0	40.0	18.7	47.6	66.4±6.2	79	8.7±1.1	12.6	14.5	15.7
50.0	50.0	18.1	32.3	50.3±4.7	54	36.5±3.1	39.6	41.6	41.2
60.0	50.0	20.9	49.5	70.4±6.6	89	34.0±2.9	37.9	36.5	33.6
80.0	50.0	11.9	57.2	69.1±6.5	58	23.6±2.2	31.7	32.2	30.5
100.0	50.0	12.6	66.7	79.3±7.5	79	16.7±1.7	25.2	25.5	26.0
120.0	50.0	18.5	59.9	78.4±7.4	78	13.8±1.5	19.6	20.4	22.7
60.0	60.0	15.2	43.0	58.2±5.5	61	31.1±2.7	37.5	40.0	39.7
70.0	60.0	16.8	64.0	80.8±7.6	87	26.3±2.4	33.5	33.2	37.3
90.0	60.0	10.5	75.6	86.2±8.1	88	17.4±1.7	23.5	23.6	23.6
110.0	60.0	20.1	79.4	99.5±9.4	92	16.3±1.7	22.3	20.9	21.5
70.0	70.0	8.4	50.7	59.1±5.6	57	22.5±2.1	36.0	31.5	34.6
80.0	70.0	8.7	99.2	107.9±10.1	106	18.1±1.8	27.2	29.8	28.0
100.0	70.0	12.0	84.1	96.1±9.0	100	16.4±1.7	23.3	24.9	21.2
80.0	80.0	1.7	56.9	58.6±5.5	54	2.5±0.5	4.6	9.6	6.1
90.0	80.0	4.4	92.9	97.2±9.1	110	11.5±1.3	18.2	19.5	14.6
90.0	90.0	21.0	142.0	162.9±15.3	162	25.7±2.3	31.7	32.5	29.8

signals at $\sqrt{s} = 206\,\text{GeV}$ was verified to be small compared to all other uncertainties.

- **Monte Carlo Statistics** For a typical point in the Monte Carlo test mass grid, the MC statistical error on the signal rate is 7 %, but it is larger for scenarios for which both m_h and m_A are small, due to the lower signal efficiency for such scenarios. For nearly all scenarios, the MC statistical uncertainty on the background rate is between 1.5 % and 3 %, but for signals when either m_h or m_A is low, it can be as large as 5 %. An overall uncertainty of 7 % and 3 % is taken for the signal and background rates, respectively.
- **Jet Energy Resolution** The jet energy resolution is uncertain by about 3–5 % in the barrel region and approximately 15 % in the endcap regions. Uncertain jet energy resolution results in approximately a 5 % uncertainty on both the signal and background rates. These errors are obtained by comparing Z^0 calibration data with the corresponding Monte Carlo simulations.
- **Jet Energy Scale** The jet energy scale is uncertain at the 1 % level. The corresponding uncertainty on the rate of events passing the likelihood cuts is approximately 2 % for both the signal and the background.
- **Jet Angle Resolution** A 22 mrad angle resolution uncertainty in both θ and ϕ results in an uncertainty on the rate of events passing the likelihood cuts that is approximately 1 % for both the signal and the background.
- **Interpolation Uncertainty** To test the reliability of the interpolation procedure, one of the Monte Carlo signal point on the grid is deleted, and the interpolation

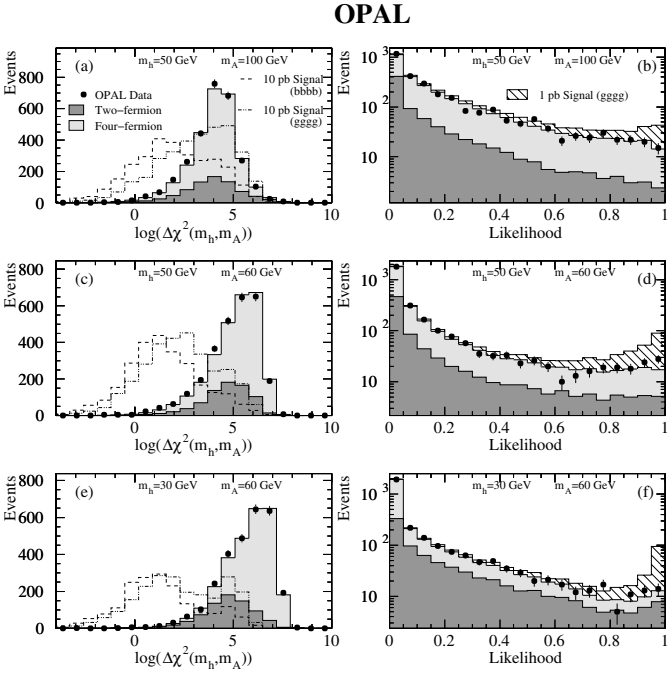

Fig. 3. Distributions of the $\log(\Delta\chi^2(m_\mathrm{h}, m_\mathrm{A}))$ variable and the likelihood output variable for three test-mass hypotheses, $(m_\mathrm{h},\ m_\mathrm{A})$=(50 GeV, 100 GeV), (50 GeV, 60 GeV), and (30 GeV, 60 GeV). OPAL data are shown with the points, light histograms show the four-fermion Standard Model background expectations, and dark histograms show the two-fermion ($\mathrm{q\bar{q}}$) Standard Model background expectations. The two background rates are shown stacked in all histograms. In the likelihood histograms, a 1 pb signal assumed to decay to gggg is shown with the hatched histograms, added on top of the background sum. For the $\log(\Delta\chi^2(m_\mathrm{h}, m_\mathrm{A}))$ distributions, a 10 pb signal assumed to decay to $\mathrm{b\bar{b}b\bar{b}}$ is shown with dot-dashed histograms which are not added to the background, while a 10 pb signal assumed to decay to gggg is shown with dotted histograms, also not added to the background

procedure is used to replace it. This process is repeated for all MC grid points not on the edges. Using the differences found in the selection rates, an uncertainty of 3.5 % is assigned to the signal efficiency and an uncertainty of 4 % is assigned to the background rate due to interpolation errors.

– **Two- and Four-Fermion Cross-Section** Nearly all of the background in scenarios near the expected limit is from four-fermion production. It is dominated by $\mathrm{e^+e^-}\to\mathrm{W^+W^-}$ production, although $\mathrm{e^+e^-}\to\mathrm{Z^0Z^{0(*)}}$ contributes as well. A 2 % uncertainty is assessed on the production cross-section of these events [32]. In comparison, the two-fermion ceoss–section uncertainty is negligible [33].
– **Monte Carlo Background Sample Comparison** The KK2F Monte Carlo generator, using PYTHIA as the parton shower and hadronisation model, was used to generate the central values for the $\mathrm{q\bar{q}}$ background rates. These rates were compared to the same KK2F sample but re-hadronised with HERWIG, and also with a sample generated entirely with PYTHIA. KORALW was used to generate the qqqq, the $\mathrm{q\bar{q}}\ell^+\ell^-$ and the $\mathrm{qq}\ell\nu_\ell$ background rate central values, and grc4f was used as the comparison generator. An uncertainty of 5.4 % is assessed on the background rates passing the likelihood cuts.

When all uncertainties are added in quadrature, the systematic error on the background rate is 9.4 % and the systematic error on the signal rate is typically 9.6 %, with larger values for the signal systematic uncertainty for scenarios with low efficiency, due to the Monte Carlo statistical uncertainty.

The correlations between the signal and background uncertainties and between the different data taking periods are taken into account. The Monte Carlo statistical error affects the signal and background predictions and are uncorrelated between energies, and also between signal and background. The other uncertainties are correlated between centre-of-mass energies.

3.4 Comparison between data and simulation

The distribution of the likelihood is used directly as the input to the limit calculation. The presence of systematic uncertainties on the background rate, including bins with low expected signal-to-background ratios, reduces the sensitivity of the search, requiring the lower cut of 0.8 on the likelihood. Table 3 lists the numbers of events passing the likelihood cut for each of the test masses on the Monte Carlo grid, the expected backgrounds, and the expected signal efficiencies for the $\mathrm{h^0A^0}\to$ gggg decay hypothesis. The signal efficiencies are also calculated separately for the $\mathrm{c\bar{c}c\bar{c}}$, $\mathrm{b\bar{b}b\bar{b}}$, and the $\mathrm{b\bar{b}c\bar{c}}$ decay hypotheses. For nearly all test mass combinations, the $\mathrm{h^0A^0}\to$ gggg hypothesis yields the least efficiency, and for the remainder, the differences are within the uncertainties.

4 Confidence level calculation

The confidence levels are derived from a test statistic [34, 35], Q, which is defined such that Q quantifies the compatibility of the data with two hypotheses: a) the background hypothesis, and b) the signal+background hypothesis. The confidence levels are computed from the observed Q-value, Q_obs, and from its probability distributions obtained from a large number of simulated experiments under these two hypotheses.

The results of the different search channels are expressed in bins of discriminating variables defined in the individual searches (e.g. mass, likelihood, neural network output, etc.). The ratio $Q = \mathcal{L}_\mathrm{s+b}/\mathcal{L}_\mathrm{b}$ of the binned likelihoods for the two hypotheses is chosen as the test statistic. The confidence level for the background hypothesis, $\mathrm{CL_b}$, is defined as the probability to obtain values of Q not larger than Q_obs, given a large number of hypothetical experiments with background processes only, $\mathrm{CL_b} = P(Q \le Q_\mathrm{obs}|\mathrm{background})$. Similarly, the confidence level for the signal+background hypothesis, $\mathrm{CL_{s+b}}$, is defined

as the probability to obtain values of Q not larger than observed, given a large number of hypothetical experiments with signal and background processes, $CL_{s+b} = P(Q \leq Q_{obs}|\text{signal} + \text{background})$. In principle, CL_{s+b} could be used to exclude the signal+background hypothesis, given a model for Higgs boson production. However, in case of a downward fluctuation of the data, this procedure would allow an experiment to exclude a signal hypothesis to which it has no sensitivity. Therefore the ratio $CL_s = CL_{s+b}/CL_b$ is used. It is always greater than CL_{s+b} and the limit obtained in this way is thus conservative. A hypothesis is considered to be excluded at the 95 % confidence level if the corresponding value of CL_s is less than 0.05.

The expected confidence levels are obtained by replacing the observed data with a large number of simulated events for the background only or signal+background hypotheses.

The effect of systematic uncertainties for the individual channels is calculated using a Monte Carlo technique. The signal and background estimations are varied within the bounds of the systematic uncertainties, assuming Gaussian distributions of the uncertainties. Correlations are taken into account. These variations are convoluted with the Poisson statistical variations of the assumed signal and background rates in the confidence level calculation. The effect of systematic uncertainties on the exclusion limits generally turns out to be small.

5 Model independent interpretation

To determine whether a signal was observed, we compute $1 - CL_b$ for each point in the (m_h, m_A) plane in the search region. Given the mass resolution of approximately 3 GeV for the sum of m_h and m_A, and approximately 7 GeV for the difference between m_h and m_A, there are approximately 160 independent searches, each of which may have an excess or deficit, diluting the significance of $1 - CL_b$. Thus, more than one independent excess in $1 - CL_b$ is expected at the percent level. Figure 4 shows $1 - CL_b$ on a logarithmic scale as a function of m_h and m_A. Nowhere is $1 - CL_b$ below 1%. The search for $e^+e^- \to h^0A^0 \to$hadrons is sensitive to models for which the production cross-section exceeds 200 fb for $\sqrt{s}$ between 189 GeV and 206 GeV. For 100% decays to hadrons and $c^2 = 1$, this corresponds to $m_h + m_A \sim 130$ GeV, with only a small depenendence on $\sqrt{s}$. Monte Carlo signal samples were generated with $m_h > 30$ GeV, $m_A > 30$ GeV, and $m_h + m_A < 175$ GeV ($1 - CL_b$ is shown in this range in Fig. 4).

Since no excess of data has been observed, the flavour–independent search for $e^+e^- \to h^0A^0$, described in Sect. 3, is used to set 95 % CL upper limits on the h^0A^0 production cross-section assuming 100 % hadronic branching ratios. The cross–section for $e^+e^- \to h^0A^0$ is determined by m_h, m_A, and a scale factor c^2, defined as the ratio of the pair–production cross–section in the scenario under consideration and the reference cross–section. The coupling limit is calculated by finding the value of c^2 for which $CL_s = 0.05$, assuming both the h^0 and the A^0 to decay 100 % hadronically. Figures 5 and 6 show the 95% median

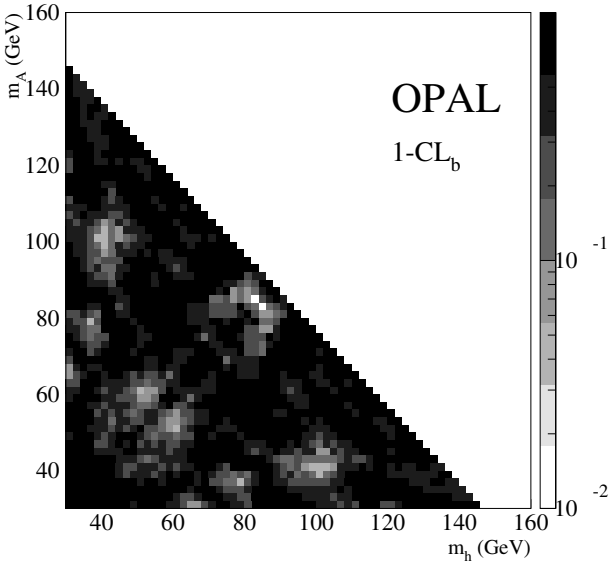

Fig. 4. The value of $1 - CL_b$ as a function of (m_h, m_A)

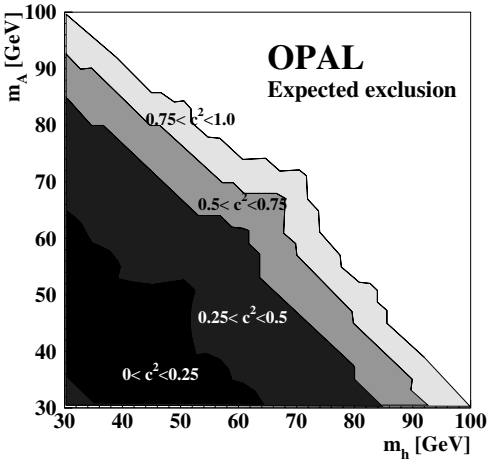

Fig. 5. The median expected limit on the coupling c^2. Both the h^0 and the A^0 are assumed to have 100% branching ratio to hadrons

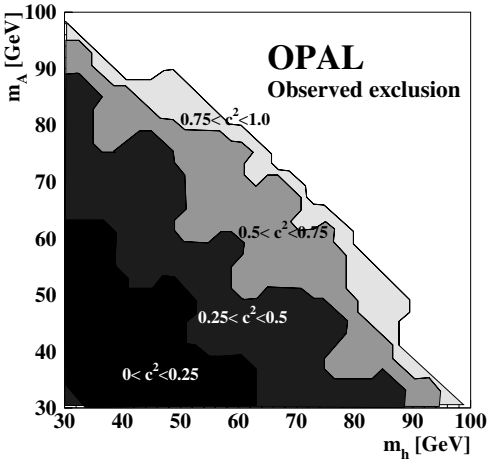

Fig. 6. The limit on the coupling c^2. Both the h^0 and the A^0 are assumed to have 100% branching ratio to hadrons

expected and observed upper limit on c^2, respectively, as a function of the test-mass hypotheses, (m_h, m_A).

The composition of the background which passes the likelihood cut depends strongly on the test-masses m_h and m_A. For low m_h and m_A, the 2f background dominates, but for scenarios near the limit, the 4f background is the most important. The signal efficiency after the likelihood cut also depends strongly on the mass hypotheses. For $m_h \sim m_A \sim 30\,\text{GeV}$, the 2f background is quite large and closely mimics the signal. Only a very small fraction of the signal and of the background passes the likelihood selection requirement because of the reduced separation power between the signal and the background – the signal efficiency for this particular scenario is only $1.9\pm0.5\%$. This small efficiency is compensated by the large expected signal cross section for low Higgs masses. Another mass hypothesis where the signal efficiency is low is $m_h \sim m_A \sim 80\,\text{GeV}$. In this case, the W^+W^- background is dominant, and the separation between the signal and the background is poor. For this scenario, the signal cross-section is between 70 fb at $\sqrt{s}$= 189 GeV and 100 fb at $\sqrt{s}$= 206 GeV and is therefore beyond the range of sensitivity of the search. Over much of the range of tested mass hypotheses, the signal efficiency is between 20% and 30%, and signal cross-sections as low as 200 fb are excluded.

As a result of the improved sensitivity of the analysis and the inclusion of data taken at higher centre-of-mass energies in the years 1999 and 2000, the excluded domains in Fig. 6 are extended substantially beyond those obtained in [1].

6 Search channels and external constraints used in the 2HDM(II) interpretation

In this section the search channels and the external constraints used to explore the 2HDM(II) parameter space are described.

6.1 Data samples and final state topologies studied

The present study relies on the data collected by OPAL at $\sqrt{s} \approx m_Z$ and from $\sqrt{s} \approx 183\,\text{GeV}$ to 209 GeV. This paper uses existing published analyses for all but the new h^0A^0 flavour–independent channel described in Sect. 3. Channels that use b-tagging provide useful information in regions of the 2HDM(II) parameter space where the Higgs bosons are expected to decay predominantly into $b\bar{b}$ pairs. Flavour–independent channels, not using any b-tagging information, are also included in the combination in order to explore the regions at low α or low $\tan\beta$, where the decays of the h^0 and A^0 bosons into $b\bar{b}$ and $\tau^+\tau^-$pairs are suppressed. In Table 4 the references to the published OPAL papers for the direct search channels combined in the present 2HDM(II) interpretation are given, together with the corresponding centre-of-mass energies at which they were performed.

The channels used at $\sqrt{s} \approx m_Z$, 183 and 189 GeV are the same as in [1]. The integrated luminosities, the numbers of candidate events, the expected SM backgrounds and the efficiencies for each of the b-tagging (flavour–independent) h^0Z^0 channels at $192 \leq \sqrt{s} \leq 209\,\text{GeV}$ are given in Table 5

Table 4. Search channels combined in the present 2HDM(II) scan. Searches labelled $q\bar{q}$ include gg decays as well. The numbers in the table give the references to the OPAL publications where a full description of the channel can be found. Channels marked NA are not analysed. The $h^0A^0 \to q\bar{q}q\bar{q}$ analysis for the data taken in the years 1999 and 2000 is new and is described in Sect. 3 of this paper

	$\sqrt{s}$ [GeV]			
Decay topologies	m_Z	183	189	$192 \to 209$
h^0Z^0				
$b\bar{b}q\bar{q}$, $b\bar{b}\nu\bar{\nu}$, $b\bar{b}e^+e^-$, $b\bar{b}\mu^+\mu^-$, $b\bar{b}\tau^+\tau^-$	NA	[1]	[1]	[14]
$q\bar{q}\nu\bar{\nu}$, $q\bar{q}e^+e^-$, $q\bar{q}\mu^+\mu^-$, $q\bar{q}\tau^+\tau^-$	[1]	NA	[1]	[36]
$\tau^+\tau^-q\bar{q}$	[1]	[1]	[1]	[36]
$q\bar{q}q\bar{q}$	NA	NA	[1]	[36]
h^0A^0				
$q\bar{q}\tau^+\tau^-$or $\tau^+\tau^-q\bar{q}$	[1]	NA	NA	NA
$b\bar{b}b\bar{b}$, $b\bar{b}\tau^+\tau^-$or $\tau^+\tau^-b\bar{b}$	NA	[1]	[1]	[37]
$q\bar{q}q\bar{q}$	NA	NA	[1]	This paper
$m_h \geq 2m_A$, $h^0A^0 \to A^0A^0A^0$				
$b\bar{b}b\bar{b}b\bar{b}$	[1]	[1]	[1]	[37]
$m_h \geq 2m_A$ and $m_A \leq 2m_b$, $h^0Z^0 \to A^0A^0Z^0$				
$A^0 \to c\bar{c}$, $\tau^+\tau^-$, gg and $Z^0 \to \nu\bar{\nu}$, $\mu^+\mu^-$, e^+e^-	NA	NA	[38]	[38]
$m_h \geq 2m_A$, $h^0Z^0 \to A^0A^0Z^0$				
$b\bar{b}b\bar{b}q\bar{q}$, $b\bar{b}b\bar{b}\nu\bar{\nu}$	NA	[1]	[1]	[37]
$b\bar{b}b\bar{b}e^+e^-$, $b\bar{b}b\bar{b}\mu^+\mu^-$, $b\bar{b}b\bar{b}\tau^+\tau^-$	NA	[1]	[1]	NA

Table 5. The h^0Z^0 b-tagging channels for data collected in the year 1999 with $192 \leq \sqrt{s} \leq 202\,\text{GeV}$, and for data collected in the year 2000 with $200 \leq \sqrt{s} \leq 209\,\text{GeV}$, respectively. The integrated luminosities ($\mathcal{L}$), the numbers of events after the final likelihood or Neural Network cut for the data and the expected background, normalised to the data luminosity are shown. The errors on the total background include modeling uncertainties and Monte Carlo statistics. The last column shows the detection efficiencies for a Higgs boson with m_h= 100 GeV for the year 1999 data and m_h= 115 GeV for the year 2000. Since the four-jet channel relies on a mass-dependent analysis, the numbers quoted in the table are given as an example for m_h= 90 GeV (100) for the year 1999 (2000) data. For the four-jet channel, the efficiency is computed only for $h^0 \to b\bar{b}$ decays, while for the missing-energy, electron and muon channels the efficiency is for all decays of the h^0, assuming SM branching fractions. For the tau channel, the efficiency is quoted for the processes $Z^0h^0 \to \tau^+\tau^-(h^0 \to \text{all})$ or $Z^0h^0 \to q\bar{q}\tau^+\tau^-$ assuming SM branching fractions

Channel $h^0Z^0 \to$	$\mathcal{L}$ [pb^{-1}]	Data	Total bkg	eff [%]
$192 \leq \sqrt{s} \leq 202$ GeV				
$b\bar{b}q\bar{q}$ ($m_h = 100$ GeV)	217.0	30	28.8 ± 4.2	42.0
$b\bar{b}\nu\bar{\nu}$	212.7	10	13.9 ± 1.6	46.9
$b\bar{b}\tau^+\tau^-/\tau^+\tau^-q\bar{q}$	213.6	5	5.1 ± 0.8	25.8
$b\bar{b}e^+e^-$	214.1	3	4.1 ± 0.7	57.2
$b\bar{b}\mu^+\mu^-$	213.6	6	3.3 ± 0.5	62.5
$200 \leq \sqrt{s} \leq 209$ GeV				
$b\bar{b}q\bar{q}$ ($m_h = 115$ GeV)	207.3	20	17.5 ± 2.6	40.0
$b\bar{b}\nu\bar{\nu}$	207.2	11	8.9 ± 1.0	40.7
$b\bar{b}\tau^+\tau^-/\tau^+\tau^-q\bar{q}$	203.6	5	4.5 ± 0.7	25.6
$b\bar{b}e^+e^-$	203.6	1	3.6 ± 0.7	52.9
$b\bar{b}\mu^+\mu^-$	203.6	4	3.4 ± 0.5	59.2

(Table 6). The detection efficiencies quoted in Tables 5 and 6 are given as examples for specific values of m_h. The integrated luminosities, the numbers of candidate events, the expected SM backgrounds and the efficiencies for the most relevant b-tagged h^0A^0 channels are given in Table 7.

When scanning the parameter space the efficiency is calculated for each point in the (m_h, m_A) plane for each of the final states considered. All direct search channels

Table 6. The h^0Z^0 flavour–independent channels for data collected in 1999 with $192 \leq \sqrt{s} \leq 202\,\text{GeV}$ and in year 2000 with $200 \leq \sqrt{s} \leq 209\,\text{GeV}$: the integrated luminosities ($\mathcal{L}$), the numbers of events after the final likelihood or Neural Network cut for the data and the expected background, normalised to the data luminosity. The errors on the total background include modeling uncertainties and Monte Carlo statistical errors. The last column shows the detection efficiency for a Higgs boson decaying to quark or gluon pairs with $m_h = 90\,\text{GeV}$ and with $m_h = 100\,\text{GeV}$ for data collected in year 1999 and 2000, respectively. Since the four-jet channel relies on a mass-dependent analysis, the numbers quoted in the table are given as an example for $m_h = 90\,\text{GeV}$ (100) for the year 1999 (2000) data

Channel $h^0Z^0 \to$	$\mathcal{L}$ [pb^{-1}]	Data	Total bkg.	eff [%]
$192 < \sqrt{s} < 202$ GeV				
$q\bar{q}q\bar{q}$ ($m_h = 90$ GeV)	217.0	290	290.6 ± 37.7	52.0
$q\bar{q}\nu\bar{\nu}$	212.7	68	70.8 ± 10.8	45.2
$q\bar{q}\tau^+\tau^-/\tau^+\tau^-q\bar{q}$	213.7	1	4.6 ± 0.8	27.1
$q\bar{q}e^+e^-$	214.1	13	8.3 ± 2.5	58.6
$q\bar{q}\mu^+\mu^-$	213.6	7	7.6 ± 1.5	64.8
$200 < \sqrt{s} < 209$ GeV				
$q\bar{q}q\bar{q}$ ($m_h = 100$ GeV)	207.3	263	235.3 ± 28.2	55.0
$q\bar{q}\nu\bar{\nu}$	208.2	55	62.3 ± 2.2	48.4
$q\bar{q}\tau^+\tau^-/\tau^+\tau^-q\bar{q}$	205.3	2	4.2 ± 0.8	21.0
$q\bar{q}e^+e^-$	208.2	10	8.3 ± 2.5	58.8
$q\bar{q}\mu^+\mu^-$	207.8	9	7.4 ± 1.4	62.4

are combined following the statistical method described in Sect. 4, increasing the Higgs boson discovery potential and, in case of absence of signal, the exclusion power.

6.2 External constraints

In addition to the combination of the direct search channels, the following external constraints are applied in every parameter space point considered:

(a) A powerful experimental constraint on extensions of the SM is the determination of the total width of the Z^0 boson, Γ_Z, at LEP [39]. Any possible excess width obtained when subtracting the predicted SM width from

Table 7. The h^0A^0 channels for data collected in the years 1999 and 2000. The integrated luminosities ($\mathcal{L}$), the numbers of events after the final likelihood or Neural Network cut for the data and the expected background, normalised to the data luminosity. The errors on the total background include modeling uncertainties and Monte Carlo statistics. The last column shows the detection efficiency for the mass combination given in the second column

Channel $h^0A^0 \to$	(m_h, m_A) [GeV]	$\mathcal{L}$ [pb^{-1}]	Data	Total bkg	eff [%]
$192 \leq \sqrt{s} \leq 209$ GeV					
$b\bar{b}b\bar{b}$	(90, 90)	424.3	22	19.9 ± 2.01	49.4
$b\bar{b}\tau^+\tau^-/\ \tau^+\tau^-b\bar{b}$	(90, 90)	417.2	13	13.2 ± 2.02	42.5
$b\bar{b}b\bar{b}b\bar{b}$	(100, 40)	424.3	22	19.9 ± 2.01	59.4
$199 \leq \sqrt{s} \leq 209$ GeV					
$b\bar{b}b\bar{b}\nu\bar{\nu}$	(100, 40)	207.2	19	17.2 ± 2.30	66.0
$b\bar{b}b\bar{b}q\bar{q}$	(100, 40)	207.3	20	17.5 ± 2.6	31.5

the measured value of Γ_Z, $\Delta\Gamma_Z$, can be used to place upper limits on the cross–section of Z^0 decaying, as in the 2HDM, into final states with h^0 and A^0 bosons [40]. The maximum additional contribution to the total Z^0 width that is compatible with the measured width at 95 % CL is $\Delta\Gamma_Z = 6.5\,\mathrm{MeV}$, obtained from the latest LEP combined Z^0 lineshape results [25]. An expected increase of the partial width of the Z^0 is evaluated for each scanned parameter space point in the 2HDM(II); if it is found to exceed the experimental limit, the point is excluded.

(b) The decay–mode–independent search for $e^+e^- \to SZ^0$ [41], where S is any scalar particle produced in association with the Z^0 boson, provides an upper limit on the scaling factor s^2, defined as $\sigma_{SZ} = s^2\sigma^{SM}_{HZ}$, where σ_{SZ} is the production cross-section for a scalar S in association with a Z^0, and σ^{SM}_{HZ} is the expected SM cross-section for $m_S = m_{H_{SM}}$. This translates into a limit on the production cross-section in each parameter space point of the 2HDM(II) for which $\sigma_{hZ} > s^2\sigma^{SM}_{HZ}$ at 95 % CL.

(c) In regions of the 2HDM(II) parameter space for which $4 \le m_h\ (m_A) \le 12\,\mathrm{GeV}$ a special study was performed in [42], and 95 % CL limits were obtained on the Yukawa couplings of h^0 and A^0 to down-type fermions. These limits are applied as an external constraint in the scan of the 2HDM(II) parameter space described in Sect. 7.

The production of any neutral low mass scalar particle in association with the Z^0 was investigated in [43] and, for $m_h \le 9.5\,\mathrm{GeV}$, a mass-dependent upper limit on the Higgs boson production cross–section was obtained. This limit was translated in [1] into an upper limit on the production cross–section for m_h below 9.5 GeV, which was considered as an external constraint in combination with the Z^0-width constraint (item (a) in the previous list). The decay–mode–independent results included as an external constraint (item (b) in the previous list) provide better exclusion power than the upper limit on Higgs boson production cross–section obtained in [43], increasing the exclusion power in the 2HDM(II) parameter space for low m_h values. The external constraint on the Yukawa couplings extends the exclusion power to regions of the 2HDM(II) parameter space with low values of m_h and m_A and large $\tan\beta$. In general, the external constraints applied in the present study improve significantly the results that were obtained in [1].

7 Two Higgs doublet model interpretations

The 2HDM(II) interpretation of the neutral Higgs boson searches listed in the previous section is performed by scanning the parameter space of the model. Every (m_h, m_A, $\tan\beta$, α) point determines the production cross–section and the branching ratios to different final states. The 2HDM(II) parameter space covered by the present study is:

- $1 \le m_h \le 130\,\mathrm{GeV}$, in steps of 1 GeV
- $3 \le m_A \le 220\,\mathrm{GeV}$, in steps of 1 GeV;
  $300 \le m_A \le 500\,\mathrm{GeV}$, in steps of 100 GeV;
  $0.5 \le m_A \le 2.0\,\mathrm{TeV}$, in steps of 0.5 TeV
- $0.4 \le \tan\beta \le 40$, in steps of 1° in β, from $\beta = 22°$ to $\beta = 88°$ and an additional point corresponding to $\tan\beta$=40
- $\alpha = -\pi/2, -\pi/4,\ 0,\ \pi/4$, and $\pi/2$

The values of α are chosen to extend the analysis to the particular cases of maximal and minimal mixing in the neutral CP-even sector of the 2HDM(II) ($\alpha = \pm\pi/4$ and $\pm\pi/2$, respectively) and of $BR(h^0 \to b\bar{b}) = 0$ ($\alpha = 0$). Intermediate values of α have been scanned showing a smooth transition in the excluded domains. Representative values of α which cover minimal and maximal exclusion are used as a benchmark in the present study. The extreme cases $\alpha = \pm\pi/2$ are equivalent in the 2HDM(II) since the mass matrix of the CP-even neutral Higgs sector, containing the Higgs doublets, becomes diagonal. In the present study the other two free parameters of the model, m_H and $m_{H^\pm}$, are set at values of $m_H = 210\,\mathrm{GeV}$ and $m_{H^\pm} = 1\,\mathrm{TeV}$, above the kinematically accessible region at LEP. A scan over values of the masses m_H and $m_{H^\pm}$ up to 2 TeV has been performed and no change has been observed in the production cross–sections and branching ratios to final state topologies of h^0 and A^0, as expected from the theory.

In [1] models with $1 \le m_h \le 100\,\mathrm{GeV}$ (in steps of 1 GeV), $5 \le m_A \le 100\,\mathrm{GeV}$ (in steps of 1 GeV, and larger steps up to 2 TeV), $0.4 \le \tan\beta \le 58$ (in steps of 1° in β) and $\alpha = -\pi/2, -3\pi/8, -\pi/4, -\pi/8$ and 0, were considered. The present study is extended to cover scenarios with positive values of α ($\alpha = \pi/4$ and $\pi/2$), which are not allowed in the MSSM-like scenarios. Furthermore larger values of m_h and m_A are explored in this study, due to the increased sensitivity of the search channels to high m_h and m_A values: the data analysed have been collected at larger centre-of-mass energies and with larger luminosities than those in [1]. For $\tan\beta < 0.4$, the theoretical predictions become unreliable. For $\tan\beta > 40$ the width of the A^0 and h^0 becomes non-negligible. The decay–mode–independent study introduced in Sect. 6.2.[b] provides exclusion from $m_h \approx 1\,\mathrm{GeV}$ down to 1 KeV, where the limit on the cross-section scaling factor, s^2, with respect to the Standard Model Higgsstrahlung cross-section is of the order of 0.06 [41]. Below $m_A \approx 3\,\mathrm{GeV}$ radiative corrections become unstable inducing large fluctuations in the calculated cross–sections.

The `HZHA` Monte Carlo generator [16] that includes the 2HDM(II) production cross–sections and branching ratios of the Higgs particles has been used to scan the parameter space. This generator includes next-to-next-to-leading order QCD corrections and next-to-leading order electroweak corrections. The branching ratios and cross–sections obtained were cross–checked with the results of another generator [44] in which QCD corrections are computed only up to next-to-leading order. The comparison showed an agreement better than 1 % between the results of the two programs.

The results of all the individual search channels at the studied centre–of–mass energies are combined statistically to provide 95 % confidence level (CL) limits, which are extracted using the method explained in Sect. 4. By applying the external constraints discussed in Sect. 6.2 ad-

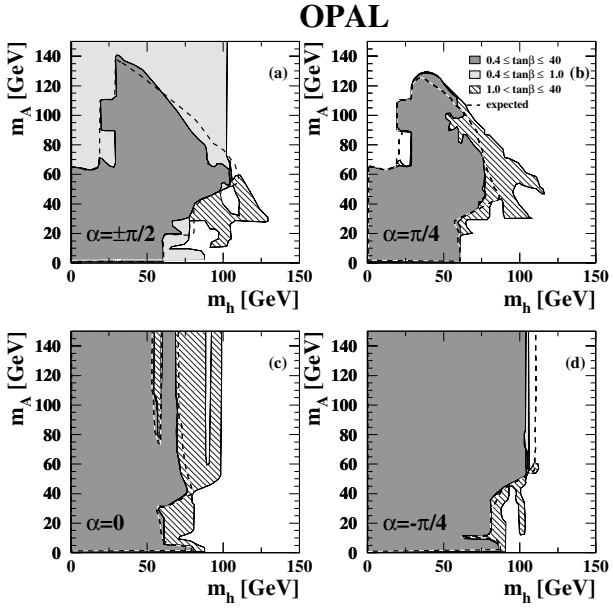

Fig. 7a–d. Excluded regions in the (m_h, m_A) plane, (a)–(d), for $\alpha = \pm\pi/2$, $\pi/4$, 0 and $-\pi/4$, respectively, together with the expected exclusion limits. A particular (m_h, m_A, α) point is excluded at 95% CL if it is excluded for $0.4 \le \tan\beta \le 40$ (darker grey region), $0.4 \le \tan\beta \le 1.0$ (lighter grey region) and $1.0 < \tan\beta \le 40$ (hatched region) for any α. Expected exclusion limits for $0.4 \le \tan\beta \le 40$ are shown as a dashed line

ditional regions of the parameter space are excluded at 95 % CL. Although the flavour–independent channels supply a unique way of investigating parameter space regions where the branching ratio $h^0 \to b\bar{b}$ or $A^0 \to b\bar{b}$ is highly suppressed (e.g., low α and $\tan\beta$ regions), they have poor sensitivity with respect to the b–tagging channels outside these regions. The use of b–tagging information substantially reduces the background coming from W^+W^- events and improves the sensitivity of observing Higgs bosons even in regions of the 2HDM(II) parameter space where only small branching ratios for $h^0 \to b\bar{b}$ are expected. The flavour–independent and b-tagging searches have candidate events in common, as is also true for the b-tag 4-jets h^0A^0 and h^0Z^0 searches. To avoid double–counting of candidate events, in each of the parameter space points only the channel that provides the best exclusion power among the ones that have some candidates in common is used for the extraction of the limits.

The direct searches for the process $e^+e^- \to h^0Z^0$ ($e^+e^- \to h^0A^0$) in the Z^0 data contribute mainly in the $m_h \le 50\,\mathrm{GeV}$ ($m_h \le 60\,\mathrm{GeV}$) region. For $\sqrt{s} \ge 189\,\mathrm{GeV}$, since the flavour–independent h^0Z^0 and h^0A^0 analyses have been performed in the mass regions $m_h \ge 60\,\mathrm{GeV}$ and $m_h,\ m_A \ge 30\,\mathrm{GeV}$, respectively, only b-tagging channels are applied below these masses. The flavour–independent analyses provide exclusion for the whole $\tan\beta$ range and for the $\tan\beta < 1$ regions for $\alpha = 0$ and $\alpha = \pm\pi/4$, respectively.

In Figs. 7a–d the excluded regions in the (m_h, m_A) plane are shown for the chosen values of α, together with the calculated expected exclusion limits. A particular (m_h, m_A, α) point is excluded at 95 % CL if it is excluded for all scanned values of $\tan\beta$. Different domains of $\tan\beta$ are studied and described below: a) $0.4 \le \tan\beta \le 40$ and b) $0.4 \le \tan\beta \le 1.0$ or $1.0 < \tan\beta \le 40$, for which enlarged excluded regions are obtained.

a) $0.4 \le \tan\beta \le 40$ (darker grey area):

- For all α values, in the region below $m_h \lesssim 10\,\mathrm{GeV}$ the sensitivity of the channels at $\sqrt{s} \approx m_Z$ is poor. The exclusion in this region is due to the application of the external constraints, as explained in Sect. 6.2, in particular to the Z width constraint. Both the h^0Z^0 and h^0A^0 production processes contribute to the natural width of the Z^0. The exclusion provided by the h^0Z^0 process is valid for any value of m_A. On the other hand, the exclusion provided by the h^0A^0 process is kinematically limited to the regions where $m_A + m_h \le m_Z$. The contribution of the h^0Z^0 production cross–section to the Z^0 width depends on the argument $(\beta - \alpha)$, and it becomes large enough for this process alone to provide exclusion in different $\tan\beta$ domains for the α values considered.
- The shape of the exclusion plot in Figs. 7a and b for $m_h < 30\,\mathrm{GeV}$ is related to the kinematic constraint on the h^0A^0 production in the Z^0 data, which for $\beta - \alpha \approx 0$ or π is the only allowed process, since the h^0Z^0 production cross–section vanishes. Since the α values are such that the condition $\beta - \alpha \approx 0$ or π is never achieved in Figs. 7c and d, the domains with $m_h + m_A > \sqrt{s}$ can be excluded by the h^0Z^0 channels. For $m_h >$ 20–30 GeV, the high energy data open a new kinematic region and are able to exclude large (m_h, m_A) areas, as can be seen in Figs. 7a and b. In the same figures the exclusion in the observed rectangular contour $20 \lesssim m_h \lesssim 30\,\mathrm{GeV}$ and $90 \lesssim m_A \lesssim 110\,\mathrm{GeV}$ is due to the recent optimisation of the $e^+e^- \to h^0A^0 \to b\bar{b}b\bar{b}$ analysis in the same kinematical region [37]. The unexcluded region $20 \lesssim m_h \lesssim 30\,\mathrm{GeV}$ and $60 \lesssim m_A \lesssim 90\,\mathrm{GeV}$ is due to a small excess in the data with respect to the expected background of about the same size as the expected signal, for $\tan\beta \approx 8$ in Fig. 7a and for $\tan\beta \approx 0.7$ in Fig. 7b, respectively.
- The (m_h, m_A) points below the semi-diagonal defined by $m_h \ge 2m_A$, for which the process $h^0 \to A^0A^0$ is kinematically allowed, can only be excluded by the high energy channels for restricted $\tan\beta$ ranges depending on the α values examined. For very low values of $\tan\beta$ the branching ratio for $A^0 \to b\bar{b}$ vanishes, causing unexcluded regions for all values of α. However, these are excluded by the Z^0 data flavour–independent analyses below $m_h \approx 60\,\mathrm{GeV}$. The region for $m_A \le 10\,\mathrm{GeV}$ is difficult to exclude since the decay $h^0 \to A^0A^0$ is usually dominant when kinematically allowed and the A^0 cannot decay to $b\bar{b}$. Therefore the searches using b-tagging do not help in this region, while the sensitivity of the flavour–independent h^0Z^0 channels is too low to provide any exclusion. For $\alpha = 0$ and $\alpha = -\pi/4$, the exclusion in this region is obtained by using the dedicated search for the process $h^0Z^0 \to A^0A^0Z^0$ followed by $A^0 \to c\bar{c}$, $\tau^+\tau^-$, gg and $Z^0 \to \nu\bar{\nu}$, $\mu^+\mu^-$, e^+e^-. By applying the Yukawa external constraint large $\tan\beta$ values are excluded.

– The region $55 \leq m_h \leq 60\,\text{GeV}$ and $m_A \geq 75\,\text{GeV}$ for $\alpha = 0$ in Fig. 7c is not excluded for $\tan\beta \leq 1$ since for the Z^0 data the h^0Z^0 cross-section becomes too small to exclude it and most of the high energy flavour–independent channels are only efficient for domains in which $m_h \geq 60\,\text{GeV}$.
– The largest (m_h, m_A) excluded domain is for $\alpha = -\pi/4$, where most of the parameter space points accessible at LEP are excluded, as can be seen in Fig. 7d.

b) $0.4 \leq \tan\beta \leq 1.0$ (lighter grey area) and $1.0 < \tan\beta \leq 40$ (hatched area):

– In Fig. 7c, as a consequence of the variation of the h^0Z^0 production cross–section with $\tan\beta$, as discussed above, the $m_h < 10\,\text{GeV}$ and $55 \leq m_h \leq 60\,\text{GeV}$, $m_A \geq 75\,\text{GeV}$ regions are excluded for all values of m_A in the $\tan\beta > 1.0$ domain. For $\alpha = \pm\pi/2$ the $m_h < 30\,\text{GeV}$ region is excluded for all values of m_A only in the $\tan\beta \leq 1.0$ domain. In the same figure, the region $m_h \sim 90\,\text{GeV}$ and $m_A \geq 60\,\text{GeV}$ has an excess of data in the four-jet flavour–independent h^0Z^0 channel at 90 GeV and therefore cannot be excluded even for $\tan\beta \geq 1$.
– At $\alpha = 0$ and small values of $\tan\beta$ the production cross–section for the process $e^+e^- \to h^0Z^0$ is highly suppressed. For $m_h > 60\,\text{GeV}$, constraining $\tan\beta > 1.0$, larger excluded regions are obtained, as can be seen in Fig. 7c (hatched area). In the same figure, the unexcluded domain $88 \lesssim m_h \lesssim 92\,\text{GeV}$, $m_A > 60\,\text{GeV}$ for $\tan\beta > 1$ is due to the presence of candidates in the flavour–independent four-jet channel in the year 2000 data [36].
– For $\alpha = \pm\pi/2$, Fig. 7a, the region $100 \lesssim m_h \lesssim 110\,\text{GeV}$ and $35 \lesssim m_A \lesssim 50\,\text{GeV}$ is unexcluded due to the presence of candidate events in the $h^0A^0 \to b\bar{b}b\bar{b}$ and $h^0A^0 \to b\bar{b}\tau^+\tau^-$ channels in the high energy data [37].

In Fig. 8 the excluded regions in the (m_h, m_A) plane independent of α are given together with the expected exclusion limits from MC studies. A particular (m_h, m_A) point is excluded at 95 % CL if it is excluded for all scanned values of $\tan\beta$ and α. Different domains of $\tan\beta$ are shown: $0.4 \leq \tan\beta \leq 40$ (darker grey area), $0.4 \leq \tan\beta \leq 1.0$ (lighter grey area) and $1.0 < \tan\beta \leq 40$ (hatched area), for which enlarged excluded regions are obtained. A rectangular region $1 \lesssim m_h \lesssim 55\,\text{GeV}$ for $3 \lesssim m_A \lesssim 63\,\text{GeV}$ is fully excluded at 95 % CL independent of α and $\tan\beta$. The scanned $\alpha > 0$ domain is new with respect to [1] and has the effect of restricting the exclusion for $\tan\beta \leq 1$ to the kinematically accessible region for the h^0A^0 production.

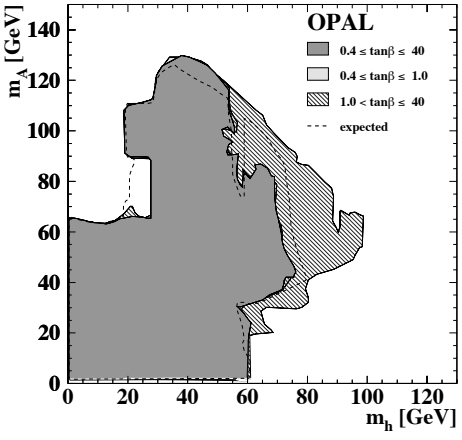

Fig. 8. Excluded (m_A, m_h) region independent of α, together with the expected exclusion limit. A particular (m_A, m_h) point is excluded at 95% CL if it is excluded for $0.4 \leq \tan\beta \leq 40$ (darker grey region), $0.4 \leq \tan\beta \leq 1.0$ (lighter grey region) and $1.0 < \tan\beta \leq 40$ (hatched region) for any α. Expected exclusion limits for $0.4 \leq \tan\beta \leq 40$ are shown as a dashed line

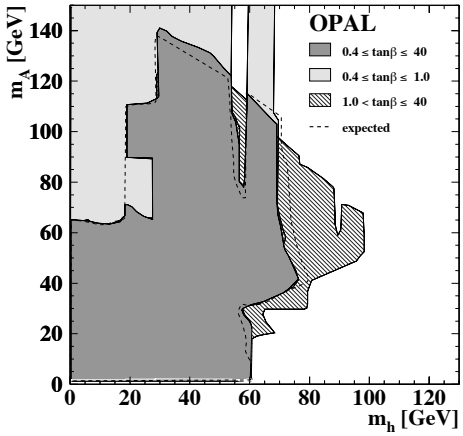

Fig. 9. Excluded (m_A, m_h) region for $-\pi/2 \leq \alpha \leq 0$, together with the expected exclusion limit. A particular (m_A, m_h) point is excluded at 95% CL if it is excluded for $0.4 \leq \tan\beta \leq 40$ (darker grey region), $0.4 \leq \tan\beta \leq 1.0$ (lighter grey region) and $1.0 < \tan\beta < 40$ (hatched region). Expected exclusion limits for $0.4 \leq \tan\beta \leq 40$ are shown as a dashed line

For completeness, the excluded regions in the (m_h, m_A) plane for $\alpha \leq 0$ are given together with the calculated expected exclusion limits, is shown in Fig. 9. The present study considerably extends the excluded (m_h, m_A) domain for negative values of α when compared with the study published in [1]. The previously excluded region of $1 \lesssim m_h \lesssim 44\,\text{GeV}$ and $12 \lesssim m_A \lesssim 56\,\text{GeV}$ is now enlarged to $1 \lesssim m_h \lesssim 55\,\text{GeV}$ and $3 \lesssim m_A \lesssim 63\,\text{GeV}$, for all $\tan\beta$ values for negative α.

In Figs. 10a–d the excluded regions in the $(\tan\beta, m_h)$ plane are shown for the chosen values of α, together with the calculated expected exclusion limits. A particular $(m_h, \tan\beta, \alpha)$ point is excluded at 95 % CL if it is excluded for all scanned values of m_A. There are two regions shown, the whole domain $3\,\text{GeV} \leq m_A \leq 2\,\text{TeV}$ (darker grey area) and a restricted domain for which $3 \leq m_A \leq 60\,\text{GeV}$ (lighter grey area). The exclusion contours for $m_A \leq 60\,\text{GeV}$ are larger for all α values, and entirely contain the $3\,\text{GeV} \leq m_A \leq 2\,\text{TeV}$ excluded areas.

In Fig. 10b the region $\tan\beta \approx 1$ is unexcluded due to the suppression of the h^0Z^0 production cross–section as $\beta - \alpha \approx 0$, while relatively low values of $\tan\beta$ can be excluded for $1 \leq m_h \leq 60\,\text{GeV}$ (darker grey area). Restricting the values of m_A to be lower than 60 GeV improves the exclusion since the kinematical limit for h^0A^0 production mechanism is never reached.

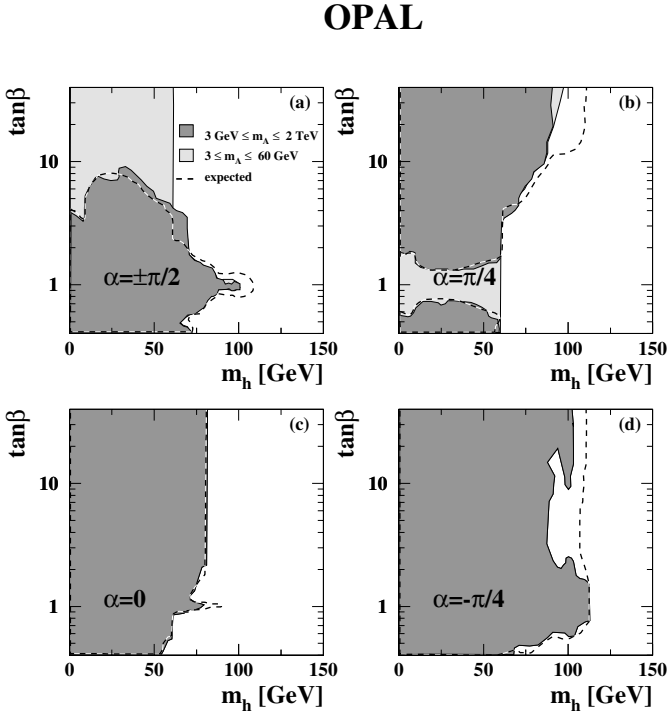

Fig. 10. Excluded regions in the (tanβ, $m_{\rm h}$) plane, **a**–**d**, for α= $\pm\pi/2$, $\pi/4$, 0 and $-\pi/4$, respectively, together with the expected exclusion limits. A particular ($m_{\rm h}$, tanβ, α) point is excluded at 95% CL if it is excluded for all scanned values of $m_{\rm A}$. The two regions shown correspond to the whole domain 3 GeV $\leq m_{\rm A} \leq$ 2 TeV (darker grey area) and a restricted domain for which $3 \leq m_{\rm A} \leq 60$ GeV (lighter grey area). The exclusion regions for $m_{\rm A} \leq 60$ GeV entirely contain the 3 GeV $\leq m_{\rm A} \leq$ 2 TeV excluded areas. Expected exclusion limits are shown for 3 GeV $\leq m_{\rm A} \leq$ 2 TeV (dashed line)

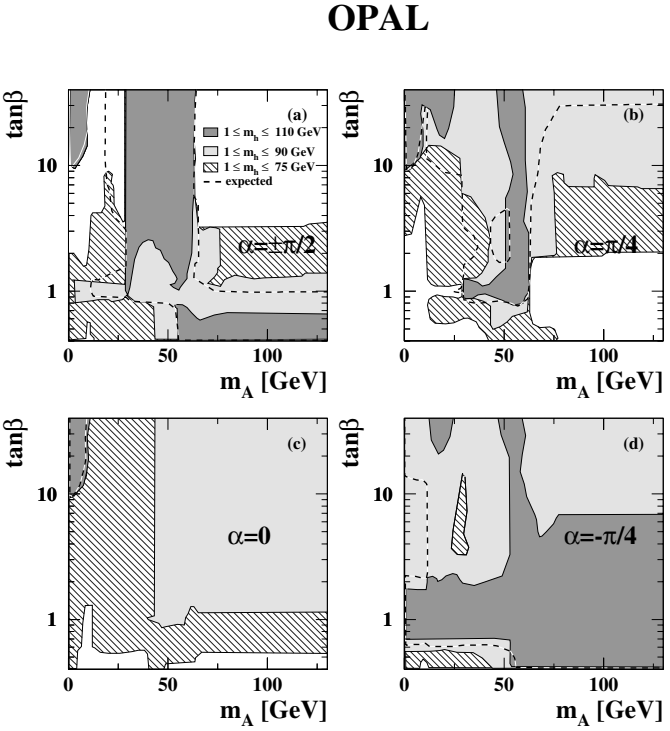

Fig. 11. Excluded regions in the ($m_{\rm A}$, tanβ) plane, **a**–**d**, for α= $\pm\pi/2$, $\pi/4$, 0 and $-\pi/4$, respectively, together with the calculated expected exclusion limits. A particular ($m_{\rm A}$, tanβ, α) point is excluded at 95% CL if it is excluded for all scanned values of $m_{\rm h}$. The three contours correspond to $1 \leq m_{\rm h} \leq 110$ GeV (darker grey area) and $1 \leq m_{\rm h} \leq 90$ GeV (lighter grey area). Expected exclusion limits are shown for $1 \leq m_{\rm h} \leq 110$ GeV (dashed line)

In Fig. 11 the excluded regions in the ($m_{\rm A}$, tanβ) plane are shown for different values of α, together with the expected exclusion limits. A particular ($m_{\rm A}$, tanβ, α) point is excluded at 95 % CL if it is excluded for all scanned values of $m_{\rm h}$. There are three regions shown, corresponding to different $m_{\rm h}$ domains that are subsets of one another, namely: $1 \leq m_{\rm h} \leq 110$ GeV (darker grey area), $1 \leq m_{\rm h} \leq 90$ GeV (lighter grey area) and $1 \leq m_{\rm h} \leq 75$ GeV (hatched area). The lower the $m_{\rm h}$ upper value analysed, the larger the excluded ($m_{\rm A}$, tanβ) region.

In Figs. 11a, b and c for $m_{\rm A} < 10$ GeV and tan$\beta > 10$ the excluded domains are a direct application of the Yukawa external constraint.

Figures 11a and b and Figs. 10a and b show a similar behaviour in the tanβ excluded domains: for $\alpha = \pm\pi/2$ ($\alpha = \pi/4$) mostly low (large) tanβ values are excluded.

In Fig. 11c for $1 \leq m_{\rm h} \leq 90$ GeV the area with $m_{\rm A} >$ 45 GeV and tan$\beta > 1$ is excluded as expected from the tan$\beta > 1$ contour in Fig. 7c. In Fig. 11d the unexcluded region in the dark grey contour for small tanβ and $m_{\rm A} <$ 50 GeV corresponds to the unexcluded region under the semidiagonal in Fig. 7d. As can be seen in Fig. 11d for $1 \leq m_{\rm h} \leq 90$ GeV, the area $24 < m_{\rm A} < 32$ GeV for $3 <$ tan$\beta < 14$ is not excluded, but it is excluded when $1 \leq m_{\rm h} \leq 75$ GeV as inferred from Fig. 7d.

In Figs. 11b and d for $1 \leq m_{\rm h} \leq 110$ GeV the area $10 < m_{\rm A} < 25$ GeV for tan$\beta > 20$ is excluded thanks to the optimisation of the $e^+e^- \to h^0A^0 \to b\bar{b}b\bar{b}$ analysis in the same kinematical region [37].

8 Conclusions

New limits on the h^0A^0 pair-production cross-section are obtained by the application of a new flavour–independent h^0A^0 analysis at the highest LEP energies. A lower bound at 95 % CL is extracted along the diagonal at $m_{\rm h} \approx m_{\rm A} \approx$ 71 GeV for $c^2 = 1$ assuming 100 % branching fraction to hadrons. The limit obtained by using the b-tagging analysis [37] and assuming 100 % decays into b-quarks, is at $m_{\rm h} \approx m_{\rm A} \approx 81$ GeV for $c^2 = 1$.

A general analysis of the 2HDM(II) with no CP violation and no additional particles besides those of the SM and the five Higgs bosons has been performed using the Z^0, 183 and 189 GeV data together with the high energy data taken by OPAL in the years 1999 and 2000 at $\sqrt{s} = 192 - -209$ GeV. Large areas of the parameter space of the model have been scanned. In the scanning procedure the dependence of the production cross–sections and branching ratios on the angles α and β, calculated with next-to-next-to-leading or-

der QCD corrections and next-to-leading order electroweak corrections, has been considered.

In addition to the OPAL b–tagging analyses, flavour–independent channels for both the Higgsstrahlung process, $e^+e^-\to h^0Z^0$, and the pair–production process, $e^+e^-\to h^0A^0$, have been analysed, providing access to regions of parameter space in the 2HDM(II) where h^0 and A^0 are expected to decay predominantly into up–type quarks and gluons (e.g. $\alpha \approx 0$).

The 2HDM(II) parameter space scan, for $1 \leq m_h \leq 130\,\text{GeV}$, $3\,\text{GeV} \leq m_A \leq 2\,\text{TeV}$, $-\pi/2 \leq \alpha \leq \pi/2$ and $0.4 \leq \tan\beta \leq 40$, leads to large regions being excluded at the 95 % CL in the (m_h, m_A) plane as well as in the (m_h, $\tan\beta$) and (m_A, $\tan\beta$) projections. The region $1 \lesssim m_h \lesssim 55\,\text{GeV}$ and $3 \lesssim m_A \lesssim 63\,\text{GeV}$ is excluded at 95 % CL both when restricting $\alpha \leq 0$, as in a MSSM-like scenario, and in the general 2HDM(II) case, for selected values of α which are representative of a complete α–scan.

The results obtained by adding the data taken by OPAL in the years 1999 and 2000 substantially enlarge the excluded domains in the 2HDM(II) parameter space accessible by LEP.

Acknowledgements. We particularly wish to thank the SL Division for the efficient operation of the LEP accelerator at all energies and for their close cooperation with our experimental group. In addition to the support staff at our own institutions we are pleased to acknowledge the Department of Energy, USA, National Science Foundation, USA, Particle Physics and Astronomy Research Council, UK, Natural Sciences and Engineering Research Council, Canada, Israel Science Foundation, administered by the Israel Academy of Science and Humanities, Benoziyo Center for High Energy Physics, Japanese Ministry of Education, Culture, Sports, Science and Technology (MEXT) and a grant under the MEXT International Science Research Program, Japanese Society for the Promotion of Science (JSPS), German Israeli Bi-national Science Foundation (GIF), Bundesministerium für Bildung und Forschung, Germany, National Research Council of Canada, Hungarian Foundation for Scientific Research, OTKA T-038240, and T-042864, The NWO/NATO Fund for Scientific Research, the Netherlands.

References

1. OPAL Coll., G. Abbiendi et al., Eur. Phys. J. C **18**, 425 (2001)
2. P. Higgs, Phys. Lett. **12**, 132 (1964)
3. F. Englert, R. Brout, Phys. Rev. Lett. **13**, 321 (1964)
4. G.S. Guralnik, C.R. Hagen, T.W.B. Kibble, Phys. Rev. Lett. **13**, 585 (1964)
5. J.F. Gunion, H.E. Haber, G.L. Kane, S. Dawson, The Higgs Hunter's Guide, Addison-Wesley Publishing Company, 1990
6. W. Hollik, Z. Phys C **32**, 291 (1986)
7. W. Hollik, Z. Phys C **37**, 569 (1988)
8. P. Fayet, Nucl. Phys. B **90**, 104 (1975)
9. J.F. Gunion, H.E. Haber, Nucl. Phys. B **278**, 449 (1986)
10. OPAL Coll., K. Ahmet et al., Nucl. Instrum. Methods A **305**, 275 (1991)
11. S. Anderson et al., Nucl. Instrum. Methods A **403**, 326 (1998)
12. B.E. Anderson et al., IEEE Transactions on Nuclear Science **41**, 845 (1994)
13. OPAL Coll., K. Ackerstaff et al., Phys. Lett. B **391**, 221 (1997)
14. OPAL Coll., G. Abbiendi et al., Eur. Phys. J. C **26**, 479 (2003)
15. N. Brown, W.J. Stirling, Phys. Lett. B **252**, 657 (1990); S. Catani et al., Phys. Lett. B **269**, 432 (1991); S. Bethke, Z. Kunszt, D. Soper, W.J. Stirling, Nucl. Phys. B **370**, 310 (1992); N. Brown, W.J. Stirling, Z. Phys. C **53**, 629 (1992)
16. P. Janot, G. Ganis, `HZHA` generator, Physics at LEP2, CERN 96-01, Vol.2, 309 (1996)
17. S. Jadach, B.F.L. Ward, Z. Wąs, Comp. Phys. Comm. **130**, 260 (2000)
18. S. Jadach, W. Płaczek, B.F.L. Ward, Physics at LEP2, CERN 96-01, Vol.2, 286 (1996)
19. M. Skrzypek et al., Phys. Lett. B **372**, 289 (1996)
20. J. Fujimoto et al., Comp. Phys. Comm. **100**, 128 (1997)
21. T. Sjöstrand, Comp. Phys. Comm. **82**, 74 (1994)
22. G. Marchesini et al., Comp. Phys. Comm. **67**, 465 (1992)
23. J. Allison et al., Nucl. Instrum. Methods A **317**, 47 (1992)
24. L3 Coll., P. Achard et al., Phys. Lett. B **583**, 14 (2004)
25. The LEP Coll.s ALEPH, DELPHI, L3, and OPAL, the LEP Electroweak Working Group and SLD Heavy Flavour and Electroweak Groups, CERN-EP-2003-091, hep-ex/0312023 (2003)
26. OPAL Coll., K. Ackerstaff et al., Eur. Phys. J. C **2**, 441 (1998)
27. G. Hanson et al., Phys. Rev. Lett. **35**, 1609 (1975); G. Parisi, Phys. Lett. B **74**, 65 (1978)
28. ALEPH Coll., R. Barate et al., Phys. Lett. B **447**, 336 (1999)
29. F.A. Berends, R. Pittau, R. Kleiss, Comp. Phys. Comm. **85**, 437 (1995)
30. S. Catani, M.H. Seymour, CERN-TH/96-28 (1996)
31. A.L. Read, Nucl. Instrum. Methods A **425**, 357 (1999)
32. M.W. Grünewald, G. Passarino et al., hep-ph/0005309 (2000)
33. M.Kobel, Z. Wąs et al., hep-ph/0007180 (2000)
34. T. Junk, Nucl. Instrum. Methods A **434**, 435 (1999)
35. A. Read, in 1st Workshop on Confidence Limits, CERN-2000-005 (2000)
36. OPAL Coll., G. Abbiendi et al., Phys. Lett. B **597**, 11 (2004)
37. OPAL Coll., G. Abbiendi et al., Eur. Phys. J. C **37**, 49 (2004)
38. OPAL Coll., G. Abbiendi et al., Eur. Phys. J. C **27**, 483 (2003)
39. J. Ellis, R. Peccei (eds.), Physics at LEP, G. Altarelli et al., CERN 86-02, Vol. 1, 203 (1986)
40. OPAL Coll., K. Ackerstaff et al., Eur. Phys. J. C **5**, 19 (1998)
41. OPAL Coll., G. Abbiendi et al., Eur. Phys. J. C **27**, 311 (2003)
42. OPAL Coll., R. Akers et al., Eur. Phys. J. C **23**, 397 (2002)
43. OPAL Coll., P.D. Acton et al., Phys. Lett. B **268**, 122 (1991)
44. M. Krawczyk, J. Zochowski, P. Mättig, Eur. Phys. J. C **8**, 495 (1999)